Check for updates

# Advances and challenges of metal organic frameworks (MOFs) and derivatives in photoelectrocatalytic water splitting

Xin-Jie Tian,[a] Si-Jia Guo,[a] Zheng-Yi Wu,[a] Na Xu,[a] Guanqun Han,*[b] Yong-Ming Chai[a] and Bin Dong ✱*[a]

Photoelectrocatalytic (PEC) hydrogen production technology combines the advantages of photocatalysis and electrocatalysis and utilizes solar energy to drive water splitting, which is a technology for sustainable energy systems. However, its low photocatalytic water splitting efficiency results in relatively small hydrogen production. And the cost-effectiveness of PEC water splitting technology and the overall solar energy conversion efficiency to hydrogen remains a great challenge. Metal–organic frameworks (MOFs) are porous materials created through the coordination of metal ions or clusters with organic bridging ligands *via* ligand bonds. They offer high specific surface areas, abundant metal active sites, large pore volumes, and customizable structures and compositions, making them highly favorable for applications in photoelectrocatalysis. This review discusses the advancements in photoelectrocatalytic hydrogen production technology using metal−organic frameworks (MOFs) and derivatives. It covers the principles of photoelectrocatalysis, preparation methods for MOF catalysts and strategies for performance enhancement. These strategies include improving light absorption, enhancing carrier separation efficiency, and ensuring stability. The paper also discusses the current challenges and future directions of photoelectrocatalytic water splitting technology. Overall, this review offers a thorough theoretical framework and practical insights for researchers in this field.

**Wider impact**

Photoelectrocatalytic hydrogen production technology combines the advantages of photocatalysis and electrocatalysis and utilizes solar energy to drive water splitting, which is a technology for sustainable energy systems. However, its low photocatalytic water splitting efficiency results in relatively small hydrogen production. And the cost-effectiveness of PEC water splitting technology and the overall solar energy conversion efficiency to hydrogen remains a great challenge. Metal–organic frameworks (MOFs) are porous materials created through the coordination of metal ions or clusters with organic bridging ligands *via* ligand bonds, which can promote the development of photoelectrocatalytic hydrogen production technology.

## 1. Introduction

Against the backdrop of surging global energy demand and intensifying environmental problems, the development of efficient and sustainable clean energy technologies has become an important issue in the scientific community. Among them, photoelectrocatalytic water splitting technology is considered

as one of the key ways to realize a green hydrogen energy economy by solar-driven splitting of water into hydrogen and oxygen. Electrocatalysis has high efficiency and controllability with high energy conversion rates,[1–4] but it requires continuous supply of electrical energy, low hydrogen production efficiency, high cost, and complex devices.[5–8] As a green technology for energy production and environmental remediation that directly harnesses solar energy, photocatalysis exhibits significant advantages.[9–12] However, the rapid recombination of charge carriers during the photocatalytic process leads to low catalytic activity.[13–15] In contrast, photoelectrocatalysis integrates the merits of both photocatalysis and electrocatalysis, emerging as a key technology for achieving solar-to-hydrogen energy conversion. It has been successfully applied in hydrogen

[a] *State Key Laboratory of Heavy Oil Processing, College of Chemistry and Chemical Engineering, China University of Petroleum (East China), Qingdao 266580, P. R. China. E-mail: dongbin@upc.edu.cn; Fax: +86-532-86981156; Tel: +86-532-86981156*

[b] *School of Advanced Energy, Sun Yat-sen University (Shenzhen), Shenzhen 518107, P. R. China. E-mail: hangq5@mail.sysu.edu.cn*

production, oxygen generation, carbon dioxide reduction, organic compound oxidation, and wastewater treatment.[16–19] This approach involves irradiating a semiconductor to generate electron–hole pairs, while simultaneously applying a gradient potential bias to minimize charge carrier recombination. The specific steps and basic principles are systematically described in Part 2. However, photoelectrocatalytic hydrogen production still faces low light absorption efficiency, low charge separation efficiency, and poor catalyst stability in practical applications.[20–23] In order to solve these problems, researchers have extensively studied the synthesis, modification and reaction mechanism of photoelectrocatalysts, and significant progress has been achieved.

The most commonly used photocatalysts include metal oxides, sulfides, and nitrides.[24–28] The limited light-absorbing capacity of metal oxides, the tendency of reaction kinetics to be slow, the ease of photocorrosion and chemical corrosion, and the high cost of preparation have hindered their widespread adoption.[29,30] The sensitivity of sulfide catalysts to photodegradation and oxidation leads to instability and rapid deactivation during operation, lower visible light absorption efficiency, and performance can be significantly affected by pH conditions.[31,32] Although nitride catalysts have narrow bandgaps, a narrower bandgap is often accompanied by an upward shift in the conduction band (CB) potential (reduced reducing ability) or a downward shift in the valence band (VB) potential (insufficient oxidizing ability);[33] narrow bandgaps are more prone to carrier recombination;[34] furthermore, the valence band of many narrow bandgap nitrides is primarily composed of N 2p orbitals. Under illumination, the strongly oxidizing holes generated can attack the material's own $N^{3-}$ ions or metal-nitrogen bonds, leading to structural damage (*e.g.*, $g\text{-}C_3N_4 + 6h^+ \rightarrow 3C_2N_2 + N_2\uparrow$), *i.e.*, the material itself becomes a sacrificial agent for photocatalytic oxidation, resulting in photodegradation and poor stability.[35] Synthesis and processing are technically challenging and costly, and nitrides tend to show limited selectivity for hydrogen production, often favoring other by-products, further hampering their efficiency.[36–39] Carbon-based materials catalysts tend to have low electrical conductivity and electron transfer efficiency, limiting the overall photocatalytic efficiency. They have short lifetimes under harsh reaction conditions such as high pH or high temperature. The drawbacks of these catalysts limit their wide application.[40–42]

Metal–organic framework (MOF) materials and their derivatives show great potential in photoelectrocatalysis due to their tunable pore structures, high specific surface areas and abundant active sites, and they are classified as novel materials with excellent photocatalytic functions.[43–49] MOFs are formed by the self-assembly of metal nodes with organic ligands *via* coordination bonds, and their structural flexibility and chemical designability provide unique advantages for optimizing light absorption, charge separation, and surface catalytic activity.[50–55]

Currently, research on MOF materials is showing two significant trends. On the one hand, efforts are being made to synthesize MOF materials with more complex structures. By precisely designing the combination of ligands and metal nodes,

introducing multifunctional groups, or constructing hierarchical pore structures, it is possible to finely tune the crystal structure, electronic structure, and transport properties of MOF materials, thereby endowing them with richer physicochemical properties. For example, certain MOF materials with complex topological structures can provide unique microenvironments that promote the adsorption and activation of reactant molecules, thereby enhancing the selectivity and activity of catalytic reactions.[56] On the other hand, research efforts are focused on developing MOF materials with enhanced functionality and improved stability. In terms of functional enhancement, methods such as doping with heteroatoms, loading co-catalysts, or constructing heterojunctions are employed to optimize the electronic structure of MOF materials, thereby enhancing their light absorption capacity, charge separation, and transport efficiency, and ultimately improving their photocatalytic performance. In terms of stability enhancement, appropriate synthesis methods and post-processing techniques are employed to enhance the skeletal rigidity of MOF materials, improving their resistance to factors such as light, heat, and chemical environments. This ensures that they maintain stable structure and performance during long-term photocatalytic reactions, laying the foundation for practical applications.[57]

This paper reviews the research progress of MOFs and their derivatives in photoelectrocatalytic water splitting in recent years, focusing on their preparation methods, performance optimization mechanisms such as electronic structure modulation and interfacial effects, as well as challenges such as insufficient stability and mechanism studies. The research and development of photoelectrocatalytic hydrogen production is a form of solar energy utilization, which can promote the progress of renewable energy technologies. Understanding the principles and mechanisms of photoelectrocatalysis provides references and insights for other renewable energy technologies, and by integrating experimental and theoretical research results, we aim to provide theoretical basis and technological references for the development of the next generation of high-efficiency and low-cost catalysts.

## 2. PEC water splitting fundamentals

During the photocatalytic process, upon irradiation of a photocatalyst (semiconductor) with photons whose energy exceeds its bandgap, electrons in the VB are excited to the CB. This excitation results in the formation of negative charge carriers ($e_{CB}^-$) in the CB, while leaving behind positive holes ($h_{VB}^+$) in the VB. The loss of photocatalytic efficiency is mainly due to the direct binding of $e_{CB}^-$ to $h_{VB}^+$ or $^\bullet OH$ as shown in the following equations:[54]

$$e_{CB}^- + h_{VB}^+ \rightarrow \text{photocatalyst} + \text{heat} \qquad (1)$$

$$e_{CB}^- + {}^\bullet OH \rightarrow OH^- \qquad (2)$$
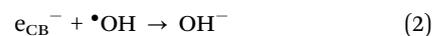
Photoelectrocatalytic technology enhances photocatalytic efficiency by integrating electrochemical techniques into the photocatalytic process.[58–60] The photoelectrocatalytic mechanism
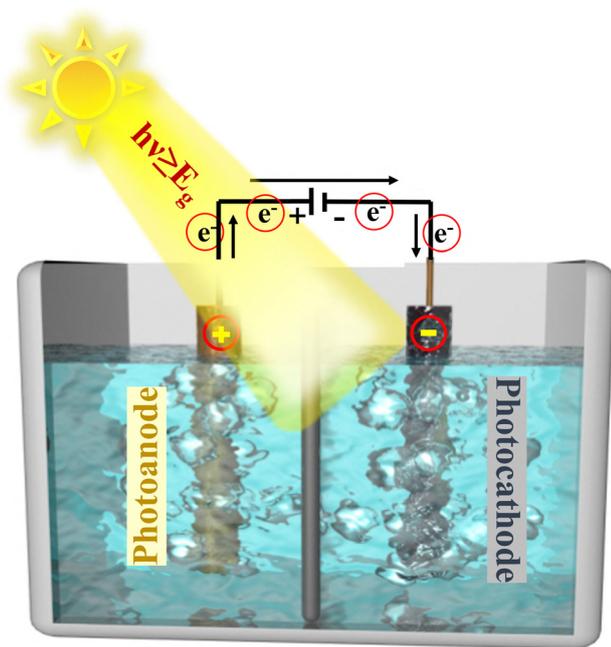
**Fig. 1** Photoelectrochemical water splitting cell.



**Fig. 2** Schematic diagram of each step of photoelectrocatalytic water splitting.

is similar to the traditional photocatalytic mechanism, based on the energy band structure theory, the light-trapping materials such as semiconductors and their co-catalysts act as photoelectrodes, and the process of HER and OER occurs on the two photoelectrodes through the reaction of photogenerated electrons and holes with water under the effect of light and applied bias voltage, as shown in Fig. 1, respectively. The difference of the principle is that the introduction of an applied electric field promotes the separation of carriers to a certain extent, which in turn improves the efficiency of the reaction. Therefore, photoelectrocatalysis is concerned with the electrochemical properties of the photoelectrodes under light conditions, where the photogenerated carriers catalyze the electrochemical reaction process at the photoelectrode–solution interface. The technology has great potential for application in various fields. The photoelectrocatalytic hydrogen production process consists of three main stages: light absorption, charge separation and reaction.[61] In the photocatalytic process, when the energy of photons (from solar energy) is larger than the semiconductor band gap, intrinsic ionization is induced at the photoelectroanode, and the absorption of photons excites electrons residing in the VB to the CB, yielding mobile electrons ($e_{CB}^-$) in the CB and leaving behind positively charged holes ($h_{VB}^+$) in the VB, which triggers the charge separation and these electron or hole pairs act as charge carriers. In photoelectrocatalytic reactions, the charge separation process is a key step in the photoelectrocatalytic reaction, which drives the subsequent chemical reactions.[62]

The steps of the photoelectrocatalytic reaction are roughly divided into three steps, as shown in Fig. 2. When light is irradiated on the photocatalyst semiconductor, the reaction of eqn (3) occurs.[63]
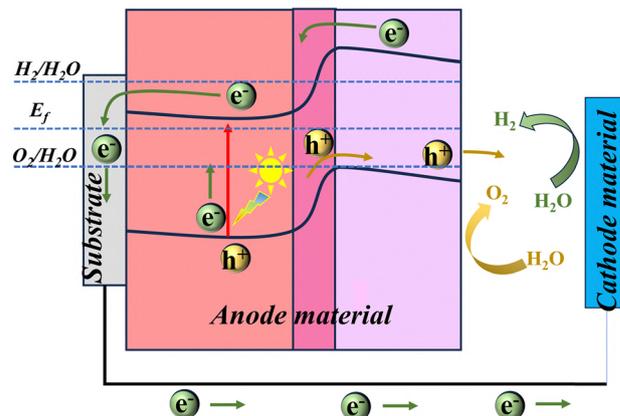
$$2h\nu \rightarrow 2e^- + 2h^+ \qquad (3)$$

When the electrolyte is in contact with the photoelectrode, the Fermi energy levels of the two need to be aligned, leading to a redistribution of charge at the interface, creating a space charge region and generating a built-in electric field. This electric field drives electrons and holes to migrate in opposite directions: holes are pushed towards the surface and OER occurs, while electrons move towards the bulk phase.[62] Water is decomposed by cavities at the photoelectrode anode, releasing gaseous oxygen (eqn (4)).[64]

$$\text{Anode: } 2h^+ + H_2O(l) \rightarrow 1/2O_2(g) + 2H^+(aq) \qquad (4)$$
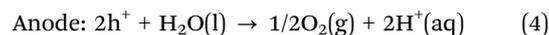
Electrons are transferred under bias through an external circuit to the photocathode, where a HER occurs, where $H^+$ ions produced due to the splitting of water then move across the electrolyte towards the cathode to be reduced and produce $H_2$ (eqn (5)).[65]

$$\text{Cathode: } 2e^- + 2H^+(aq) \rightarrow H_2(g) \qquad (5)$$
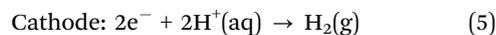
The total net reaction in a PEC cell is shown in eqn (6)[66]

$$2h\nu + H_2O(l) \rightarrow 1/2O_2(g) + H_2(g) \qquad (6)$$
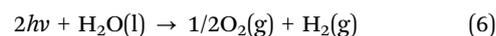
Therefore, it is known that the factors affecting photoelectrocatalytic water splitting are (1) the light absorption range, (2) the separation of electron–hole pairs and (3) the surface electrochemical reaction. To optimize the performance of photoelectrocatalytic hydrogen production, it is necessary to improve the photo-absorption capacity, carrier separation efficiency and reactivity of the photocatalyst.[67]

# 3. PEC water splitting performance evaluation parameters

In the assessment of the hydrogen evolution reaction (HER) efficiency during photoelectrochemical (PEC) water splitting, it is essential to put forward efficiency criteria and develop suitable comparative metrics for evaluating the performance

of PEC systems. It is worth noting that among the many indicators used to evaluate the performance of advanced photo-electrode materials, solar-to-hydrogen (STH) conversion efficiency is widely regarded as one of the most important, comprehensive, and practically meaningful core calibration efficiencies:

$$= \frac{j_{sc}\ (A\ m^{-2}) \times 1.23\ V \times \eta_F}{P_{solar\ AM1.5G}\ (W\ m^{-2})}$$

$$STH = \frac{mol\ H_2\ (m^{-2}\ s^{-1}) \times 237\ kJ\ mol^{-1}}{P_{solar\ AM1.5G}\ (W\ m^{-2})}$$

Among these, $j_{sc}$ is the current density of the photoelectrode at 0 V in a two-electrode setup, $P_{solar}$ is the incident power on the active photoelectrode, and AM 1.5G is the standard representation of 1 sun, equivalent to an irradiance of 100 mW cm$^{-2}$. $A$ is the illuminated electrode area, and $\eta_F$ is the Faraday efficiency for hydrogen evolution.

In photocatalytic experiments, parameters such as photocurrent density are frequently used as performance evaluation criteria. The photocurrent density $j_p$ refers to the ratio of the photocurrent produced by a photoelectrode to its illuminated area under one-sun irradiation. As a key indicator, it directly mirrors the performance of the photoelectrode and is affected by multiple factors. Specifically, it is generally determined by the light absorption rate, the separation efficiency of electron–hole pairs in the bulk phase, and the surface charge injection efficiency, while also varying with the applied bias voltage. The photocurrent density can be expressed *via* the formula below:[68,69]

$$j_p = j_{max} \times (\eta_{abs} \times \eta_{sep} \times \eta_{inj})$$

$j_p$: experimentally measured photocurrent density; $j_{max}$: maximum theoretical photocurrent density attainable by the semiconductor photocathode; $\eta_{abs}$: optical absorption efficiency of the semiconductor photocathode; $\eta_{sep}$: charge carrier separation efficiency within the semiconductor photocathode; $\eta_{inj}$: surface charge injection efficiency at the semiconductor/electrolyte interface of the photocathode.

Additionally, the photoconversion efficiency formula:[69–73]

$$\eta = \frac{j_p \times (1.23 - V)}{P_0}$$

$P_0$: incident light intensity on the photoelectrode surface. As can be seen from the formula, the photoelectric conversion efficiency $\eta$ is directly proportional to the photocurrent density $j_p$, which is not only related to the absorption and utilization efficiency of the photoelectrode, but also to the internal and interface separation efficiency of the photo-generated carriers.

Another evaluation parameter is the applied bias photon current efficiency (ABPE). ABPE primarily reflects the overall energy conversion efficiency of a photocatalytic system under applied bias. In most cases, ABPE is reported as an efficiency value for the performance of a photocathode. ABPE measures the overall conversion efficiency of light energy to hydrogen

energy, integrating light absorption, charge separation, interfacial reaction kinetics, and bias-assisted energy utilization efficiency. However, the applied bias photon-to-current efficiency (ABPE) is computed based on the voltage applied across the photoelectrode. As a modified form of STH efficiency under a specific applied voltage, ABPE requires measurements to be performed in a two-electrode setup for accurate determination.[74] The calculation of ABPE can be expressed by the following equation:

$$ABPE = \frac{j_{ph}\ (A\ m^{-2}) \times (1.23\ V - E_{app}) \times \eta_F}{P_{solar\ AM1.5G}\ (W\ m^{-2})}$$

where $j_{ph}$ denotes the photocurrent density achieved under a bias voltage $V_b$, $\eta_F$ represents the Faraday efficiency, and $P_{solar}$ is the incident solar power on the active photoelectrode area.

Subsequently, the performance metrics of PEC water splitting are briefly elaborated with respect to light absorption efficiency, charge carrier separation efficiency, and catalytic activity.

### 3.1. Light absorption efficiency

In the field of photocatalysis, the formula $J_{abs} = J_{max} \times \eta_{abs}$ is used to quantify the upper limit of a photocathode's light-capturing capacity under ideal charge separation and injection conditions, serving as the foundation for evaluating a material's intrinsic photoresponse performance. $J_{abs}$: the maximum achievable photogenerated current density (unit: mA cm$^{-2}$), representing the current density when all carriers generated by the material absorbing photons theoretically participate in the reaction; $J_{max}$: the theoretical maximum photocurrent density (unit: mA cm$^{-2}$), referring to the limiting current value under specific wavelength sunlight irradiation at 100% quantum efficiency (*i.e.*, each photon generates one electron–hole pair and all are utilized); $\eta_{abs}$: the light absorption efficiency of a semiconductor photovoltaic electrode reflects the material's ability to absorb incident light, with values ranging from 0–100%. The calculation formula is $\eta_{abs} = 1 - 10^{(-A)}$ (where $A$ is the absorbance). The absorbance of semiconductors is measured using UV-vis diffuse reflectance spectroscopy. $J_{abs}$ can be obtained by multiplying the $J_{max}$ and $\eta_{abs}$ values for each wavelength using the trapezoidal integration method.

In the photoexcitation process of semiconductor materials, the transition of valence band electrons to the conduction band follows the basic quantum model of the photoelectric effect. Within this model, the photoelectric effect can be delineated by the equation $E_k = h\nu - W$, where $E_k$ represents the maximum kinetic energy of the excited electron after it breaks free from its confinement; $h$ is Planck's constant; $\nu$ is the frequency of the incident photon; $W$ is the work function of the material, which represents the minimum energy required to excite an electron from near the Fermi level to the material's outer layer (vacuum level). To excite an electron from the valence band top to the conduction band bottom, it must obtain sufficient energy to overcome the bandgap $E_g$. At this point, $W$ is conceptually equivalent to $E_g$. This is because the excitation of electrons across the bandgap is the physical prerequisite for the generation of free carriers. Therefore, the minimum "escape work"

required for the generation of photo-generated carriers (electron–hole pairs) is the bandgap $E_g$ of the semiconductor. When $E_k = 0$, this is the minimum frequency required for light to excite carriers. Based on the formula and existing bandgap values, the minimum required frequency of light can be determined. Using the relationship between the speed of light $c$, frequency $\nu$, and wavelength $\lambda$, $c = \nu\lambda$, the threshold frequency can be converted to the corresponding maximum wavelength.[75]

By characterizing light absorption efficiency, it is possible to more specifically identify key factors contributing to the excellent catalytic performance and enhanced light absorption properties achieved by photoconductive electrode materials.

## 3.2. Carrier separation efficiency

In photocatalytic water splitting systems, even if the photoanode material exhibits excellent light absorption properties, the efficiency with which the photoexcited electron–hole pairs are spatially separated and transported to the reaction interface (charge separation efficiency, denoted as $\eta_{sep}$) often becomes a bottleneck limiting the overall performance of the catalyst. Hence, the measurement of $\eta_{sep}$ is equally crucial. In the presence of electron scavengers, photocurrent peaks associated with recombination or reverse reactions in the material can be minimized. Under such circumstances, the correlation between the photocurrent density in the electron scavenger system ($J_{ES}$) and $\eta_{sep}$ can be expressed as $\eta_{sep} \approx J_{ES}/J_{abs}$. Here, $J_{abs}$ denotes the absorbed photon flux density, while $J_{ES}$ refers to the extracted/collected charge carrier flux density. $\eta_{sep}$ allows for an intuitive assessment of the photoelectrode material's capability to generate and separate photoexcited carriers. However, the exact value of $J_{abs}$ is sometimes inaccessible,[76] making it impossible to accurately determine $\eta_{sep}$.

In such cases, we introduce several other efficiency measurement methods to assess carrier separation efficiency. The incident photon current efficiency (IPCE) is commonly used to calibrate the performance of such photoelectrodes[77,78] (compared to RHE). IPCE can be calculated based on different wavelengths in the spectrum, describing the wavelength-dependent photocurrent response, and can be calculated (in simplified form) as:

$$ \text{IPCE}\,(\lambda) = \frac{j_{ph}\,\left(\text{A m}^{-2}\right) \times 1239.8\,(\text{V nm})}{P_{\text{mono AM1.5G}}\,\left(\text{W m}^{-2}\right) \times \lambda\,(\text{nm})} $$

where $J_{ph}$ denotes the photocurrent density, $P_{mono}$ represents the monochromatic irradiance at a specific wavelength, and $\lambda$ is the wavelength of the incident light.

$$ \text{IPCE} = \eta_{abs} \times \eta_{sep} \times \eta_{inj} $$

Therefore, from the IPCE spectrum, $\eta_{sep}$ can be derived.

IPCE quantifies the overall efficiency as a function of incident wavelength, incorporating losses from reflected or transmitted photons. To evaluate the intrinsic performance of a PEC device, these optical losses must be accounted for to determine the actual efficiency. This corrected metric, known as the absorbed

photon-to-current efficiency (APCE), is calculated via:

$$ \text{APCE}\,(\lambda) = \frac{j_{ph}\,\left(\text{A m}^{-2}\right) \times 1239.8\,(\text{V nm})}{P_{\text{mono AM1.5G}}\,\left(\text{W m}^{-2}\right) \times \lambda\,(\text{nm}) \times \left(1 - 10^{-A}\right)} $$

$$ \text{APCE} = \frac{\text{IPCE}}{\eta_{abs}} = \eta_{sep} \times \eta_{inj} $$

Through APCE analysis, $\eta_{sep}$ can be accurately determined.

For investigating the electronic properties of the photoelectrode, the flat-band potential (VF) and charge carrier density (ND) can be extracted using the following expressions:[79]

$$ \frac{1}{C^2} = \frac{2}{\varepsilon\varepsilon_0 e N_d}\left(E - E_{fb} - \frac{k_B T}{e}\right) $$

In the equation, $C$ represents the space charge capacitance, $\varepsilon$ and $\varepsilon_0$ denote the dielectric constant of the semiconductor and the dielectric constant of vacuum, respectively, $e$ is the electron charge, and ND is the carrier density. The further derivation of the carrier density ND can be obtained using the following equation:[80–82]

$$ N_D = \frac{2}{\varepsilon\varepsilon_0 e}\frac{\text{d}E}{\text{d}\frac{1}{C^2}} = \frac{2}{\varepsilon\varepsilon_0 e}\frac{1}{\text{slope}} $$

Transient photocurrent is a key technology for evaluating the photoelectron-hole separation efficiency in photoelectrodes. By analyzing the response kinetics of photocurrent to pulsed light irradiation, the charge separation, recombination, and transport efficiencies can be quantitatively analyzed. The larger the photocurrent, the higher the separation efficiency.

$$ \eta_{sep} = \frac{J_{ph,\,steady}}{J_{ph,\,max}} $$

$J_{ph,\,steady}$: steady-state photocurrent (effective separation and participation of carriers in the reaction); $J_{ph,\,max}$: initial peak current under illumination (total photo-generated carriers).

In cases where the carrier separation efficiency of the fabricated photoelectrode is observed to be excessively low, targeted strategies can be employed to enhance the internal charge separation efficiency.

## 3.3. Catalytic efficiency

In the process of photocatalytic water splitting, after photo-generated charge carriers are successfully spatially separated within the material, they ultimately need to migrate to the electrode/electrolyte interface and participate in the target redox reaction on the catalyst surface. However, the accumulation of charge carriers on the surface and reaction efficiency are not spontaneously efficient but are strictly limited by the kinetics of the interface reaction. The efficiency of this critical step is typically quantified using the carrier injection efficiency ($\eta_{inj}$), which is also referred to as surface catalytic efficiency or interfacial charge transfer efficiency. $\eta_{inj}$ can be calculated by comparing the photocurrent density with or without an

electron scavenger ($\eta_{\text{inj}} = J_{\text{PEC}}/J_{\text{ES}}$). By studying $\eta_{\text{inj}}$, one can gain further insight into the performance of the prepared photoelectrode and accurately improve its defects.

While catalytic efficiency serves as a critical parameter for assessing the overall performance of a photocathode, it fails to capture the material's stability and selectivity. Faradaic efficiency (FE) is a key indicator for evaluating the reaction selectivity, stability, and charge utilization efficiency of a photocathode, directly reflecting how much of the transferred charge is effectively used for the target reaction (rather than side reactions or energy loss). FE < 100% indicates the presence of competitive side reactions, photocorrosion, and interface recombination. Given that not all photogenerated electrons participate in water splitting reactions, photocorrosion of the photoelectrode results in a Faraday efficiency (FE) significantly lower than 100%, as calculated by the equation below:

$$FE = \frac{\text{Actual amount of charge consumed to generate the target product}}{\text{Total charge passing through the reaction system}} \times 100\%$$

$$= \frac{Q_{\text{product}}}{Q_{\text{total}}} \times 100\%$$

$Q_{\text{product}}$: theoretical charge required to generate the target product (calculated according to Faraday's law); $Q_{\text{total}}$: total charge passing through the system during electrolysis $(Q_{\text{total}} = \int I \mathrm{d}t)$

For gaseous products, the formula is converted to:

$$FE = \frac{n \cdot F \cdot N_{\text{product}}}{Q_{\text{total}}} \times 100\%$$

$n$: number of electrons required to generate 1 mol of product; FF: Faraday constant ($96\,485$ C mol$^{-1}$); $N_{\text{product}}$: experimental measurement of the amount of product (mol).

Since photocatalysis is a combination of photocatalysis and electrocatalysis, the commonly used evaluation parameters for electrocatalysis are also applicable to photocatalysis. The Tafel slope is an important parameter for determining catalyst activity. It is the graphical representation of the current generated in an electrochemical cell *versus* the electrode potential of a specific metal. In simple terms, the Tafel plot describes the electrode's ability to generate current in response to changes in applied potential. It correlates reaction rate with overpotential. The smaller the Tafel slope, the faster the electron transfer.[83] Overpotential is a parameter used to assess catalyst activity. The potential applied above the equilibrium potential to initiate the reaction and release the product at the electrode is referred to as overpotential. At least 1.23 V is required to decompose water into its components, however, a substantial overpotential is generally required due to the complexity of reaction kinetics.[84] For water splitting reactions, an optimal catalyst should possess a small Tafel slope and minimal overpotential.[85]

The turnover frequency (TOF) is defined as the number of substrate molecules converted per unit time by each active site on the catalyst surface (unit: s$^{-1}$). Its core significance lies in

eliminating the interference of non-intrinsic factors such as catalyst dosage, surface area, and dispersion, directly reflecting the inherent catalytic ability of the active sites. In electrocatalytic reactions, the TOF value directly indicates the catalytic efficiency of active sites: a higher TOF value means that each active site completes more catalytic cycles per unit time, indicating stronger intrinsic catalytic activity of the catalyst. The formula for TOF is:

$$TOF = \frac{\text{Product yield per unit time}}{\text{Total number of active sites}}$$

For example, in the hydrogen evolution reaction (HER):

$$TOF_{H_2} = \frac{j \times A}{2F \times n_{\text{site}}}$$

$j$: current density, $A$: electrode area, $F$: Faraday constant, $n_{\text{site}}$: number of active sites. Electrochemical active surface area (ECSA) reflects the number of effective active sites. It refers to the effective area on the catalyst surface that can participate in electrochemical reactions, and its size is directly related to the number of active sites that can be contacted on the catalyst surface. Double-layer capacitance ($C_{\text{dl}}$) is related to the area of the electrode surface capable of storing charge and is often used to estimate ECSA, indirectly reflecting the number of active sites. A larger ECSA indicates a greater number of exposed active sites. Electrochemical impedance spectroscopy (EIS) is an evaluation parameter for analyzing the kinetic processes of electrocatalytic reactions. EIS measures the impedance response of the electrode at different AC frequencies (typically presented as a Nyquist plot), decomposing the complex electrode process into parameters such as charge transfer resistance ($R_{\text{ct}}$), solution resistance ($R_{\text{s}}$), and diffusion resistance ($Z_{\text{w}}$). Its core significance lies in revealing the kinetic bottlenecks in electrocatalytic reactions, including charge transfer rates, interfacial adsorption/desorption behavior, and mass transport limitations. Charge transfer resistance ($R_{\text{ct}}$): reflects the ease of electron transfer at the electrode/electrolyte interface. A smaller $R_{\text{ct}}$ indicates faster charge transfer rates and superior reaction kinetics. Diffusion resistance ($Z_{\text{w}}$): this parameter reflects the diffusion rate of reactants/products in the electrolyte. If $Z_{\text{w}}$ accounts for too high a proportion, it indicates that the reaction is limited by mass transport (*e.g.*, insufficient substrate concentration), and improvements can be made by optimizing the electrolyte system or catalyst structure (*e.g.*, increasing hydrophilicity). Through EIS analysis, researchers can identify the rate-limiting step of the reaction (*e.g.*, charge transfer limitation or diffusion limitation) and then optimize the

catalyst's interface structure (*e.g.*, constructing a heterojunction to promote charge transfer) or microstructure (*e.g.*, shortening the diffusion path) to enhance overall catalytic efficiency.

Additionally, the stability of photoelectrode materials constitutes another crucial parameter that demands consideration. As photoelectrode materials exposed to electrolytes for extended periods can be severely hindered by photochemical and electrochemical corrosion, which impede surface reactions. An excellent photoelectrode should maintain its performance over extended periods.[86] An important factor in the practical application of materials is their stability during electrochemical studies, which primarily depends on the properties of the electrolyte and electrode. Typically, directly preparing catalytic materials is a better strategy than coating them onto electrodes to extend the stability of test materials even in alkaline media. Material stability can be assessed using chronoamperometry, cyclic stability testing, *in situ* FTIR, XRD, and SEM analysis.[87–91]

# 4. Preparation of MOF and its derivative photoanodes

Fujita *et al.*[92] discovered the application of MOFs in catalysis in 1994. Subsequently, Alvaro *et al.*[93] demonstrated that MOFs have semiconducting properties. Yu and Mahata *et al.*[94,95] conducted a preliminary study on the preparation of MOFs with photocatalytic properties. In 2009, Mori's group reported the use of MOFs as photocatalysts for water splitting,[96,97] and found that MOFs could significantly improve the performance of the photoelectrocatalytic oxygen evolution reaction, and this discovery contributed to the rapid development of MOF-based materials for use as photocatalysts for water splitting. The structure of MOFs usually consists of organic ligands and metal centers, where the organic ligands act as supports and the metal centers have in a connections role. In the synthesis of MOFs, different organic ligands and metal centers are used to

form a desirable flexible molecular structure that can be easily modified in terms of physical and chemical properties. So far, various physical and chemical synthesis methods have been investigated, highlighting the following commonly used ones.[98]

## 4.1. Sedimentation

Deposition is a technique to transfer substances from the gas or liquid phase to a solid surface. In the preparation of MOF photocatalytic materials, MOF components, precursors or functional additives (such as semiconductor quantum dots[99] and nanoparticles[100]) are deposited onto conductive substrates using techniques such as electrochemical deposition,[101] atomic layer deposition,[102] chemical vapor deposition (CVD),[103] and sol–gel deposition.[104] This process results in the formation of a composite material exhibiting enhanced photoelectrocatalytic performance. This method is highly controllable. By adjusting parameters such as temperature,[105] sedimentation time[106] and precursor concentration,[107] the thickness, morphology and composition of MOF films can be precisely controlled. The deposition method can directly grow MOF films on complex shapes or flexible substrates (such as conductive glass,[108] carbon cloth[109] and metal oxides[110]), facilitating their integration into photocatalytic devices (such as photoelectrodes[111]). Through layer-by-layer deposition or co-deposition methods, heterojunction structures comprising MOFs and other functional materials like semiconductors[112] and conductive polymers[113] can be engineered to improve light absorption and enhance carrier separation efficiency. The n–n heterojunction composite CeBTC@FeBTC/NIF, developed by Dong *et al.*[114] was created using a two-step electrodeposition technique. This composite demonstrated a notable improvement in photocatalytic efficiency by optimizing light absorption through a distinctive structural configuration and modulation of energy bands, as shown in Fig. 3. Cardenas-Morcoso *et al.*[115] synthesized cobalt-based ZIF-67 MOF modified BiVO$_4$-based photoanodes. Heat treatment of the deposited MOF in air converted ZIF-67 into highly porous CoO$_x$ co-catalysts, which resulted in
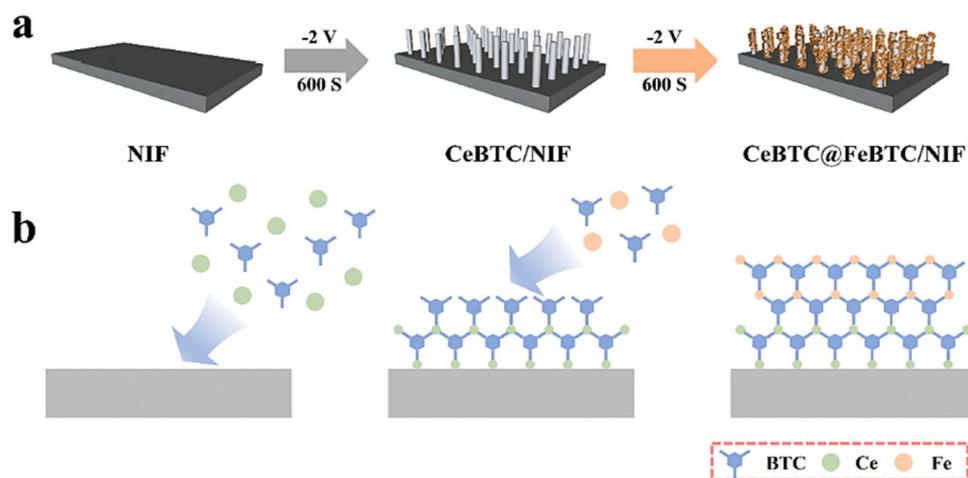


**Fig. 3** (a) Flow chart of the synthesis of CeBTC@FeBTC/NIF. (b) Diagram of the microscopic reaction during electrodeposition.[114] Copyright 2024, Elsevier.

substantial improvement in catalytic performance compared to bare $BiVO_4$ electrodes. Tang et al.[116] prepared MOF-derived $Co_3C/TiO_2$ nanocages by electrostatic adsorption deposition of nanosheets of ZIF on $TiO_2/Cu_2O$ annealed in pure argon for 6 h. The MOF was used as an electrostatic deposition method for the deposition of ZIF-67 on $TiO_2/Cu_2O$. The MOF was then used as a catalyst in a cobalt-based photoanode. The synergistic effect of the heterostructure-optimized microstructure and components significantly improved the photocurrent density and carrier separation efficiency of PEC and enhanced the water oxidation performance of PEC. Zhou et al.[117] utilized imidazolium-based cobalt (Co) complexes (Co-MIm) to cover rod-shaped $BiVO_4$ electrodes for photoelectrochemical (PEC) water splitting via a simple in situ deposition method. With the help of Co-MIm, the charge separation and injection efficiency of $BiVO_4$ photoanodes were improved. The method somewhat requires specialized equipment and is costly. Compared with traditional methods such as the solvothermal method, the deposition method (especially electrochemical deposition) may generate amorphous or low-crystallinity MOF, which reduces the porosity and exposure of catalytically active sites and affects the photovoltaic performance and low efficiency of scale-up production. Certain deposition methods have specific requirements for substrate conductivity or surface functional groups such as electrochemical deposition requires a conductive substrate,[118] limiting the binding of MOF to certain functional substrates. Post-deposition annealing or activation treatments may be required to enhance crystallinity or remove impurities, increasing process complexity.[119]

### 4.2. In situ growth method

The in situ growth method is a method to grow MOF materials with photoelectrocatalytic activity directly on the surface of a conductive substrate by chemical reaction. This method offers structural controllability. By adjusting the type and proportion of metal ions and organic ligands, as well as reaction conditions such as temperature, pH, and solvent,[120–122] the crystal structure, porosity and surface chemistry of MOFs can be precisely controlled, thereby optimizing their photocatalytic performance. The in situ-grown MOF materials are tightly bonded to the substrate surface through chemical bonding, which is not easy to come off and improves the stability and

lifetime of the materials. The preparation process is simple and usually carried out at room temperature and pressure without complex equipment, which makes it easy to operate and realize large-scale preparation. Liu[123] et al. reported the use of interfacial engineering to aid energy level modulation to improve the PEC water splitting performance of $BiVO_4$ photoanodes. An integrated photoanode $NiCo$-MOF-$CuCrO_2$-$BiVO_4$ was prepared by coupling a $CuCrO_2$ hole transport layer (HTL) and in situ growth of NiCo-MOF, as shown in Fig. 4. This integrated photoanode exhibits excellent PEC water oxidation performance and very high stability. It was shown that coupling a $CuCrO_2$ HTL and in situ growth of NiCo-MOF had a synergistic effect in improving the PEC water oxidation performance of $BiVO_4$ photoanodes. He et al.[124] reported the synthesis of $TiO_2/Ti$-MOF heterojunctions by in situ self-growth, with selective anchoring of dense Pt monoatoms, for high-efficiency photodegradation of water to produce hydrogen. The $TiO_2/Ti$-MOF heterojunction follows a Z-type electron transfer mechanism, and the MOF phase, which serves as a selective anchoring site for the co-catalyst Pt, is demonstrated to be an electron-rich region of the heterojunction, which facilitates the further participation of the photogenerated electrons separated through the heterojunction in the hydrogen precipitation reaction. The catalyst exhibited significantly enhanced visible light hydrogenolysis activity ($12.4$ mmol $g^{-1}$ $h^{-1}$). However, the in situ growth method is very sensitive to reaction conditions such as temperature, concentration, pH and so on,[125–128] which need to be precisely controlled to ensure the uniform growth and high quality of MOF materials. Limited material selectivity and the limited variety of substrate materials and functional additives currently available for the in situ growth method may limit its application in some specific areas. The yield of the in situ growth method may be lower compared to hydrothermal and solvothermal methods, etc., and further optimization is needed to improve the preparation efficiency.

### 4.3. Solvothermal

Solvothermal synthesis is the predominant approach for preparing MOFs. In this technique, metal salts and organic linkers are dissolved in a mixed solvent of organic and aqueous phases, followed by a reaction conducted within a sealed vessel at elevated temperatures ($100–500\ ^\circ$C) for 12–48 hours. During this process,



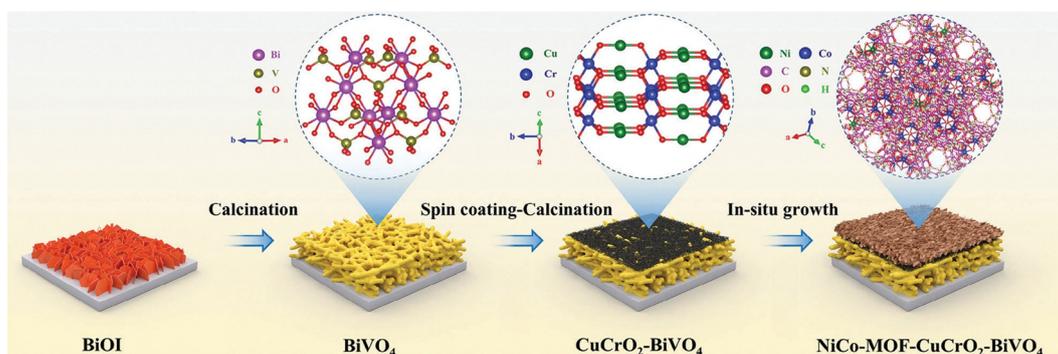**Fig. 4** Schematic synthesis route of the NiCo-MOF-$CuCrO_2$-$BiVO_4$ photoanode.[123] Copyright 2025, Wiley.

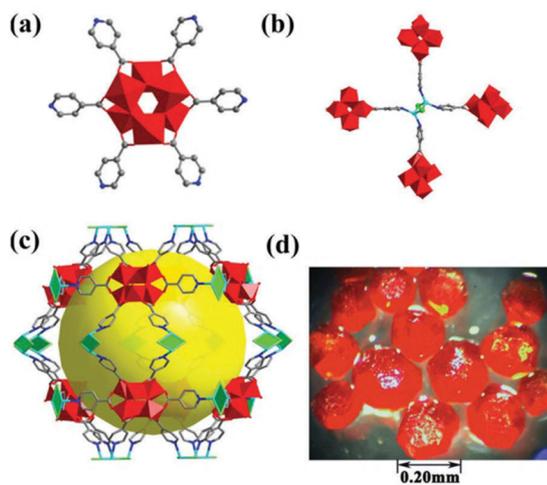**Fig. 5** (a) Structure of the hexagon-shaped unit {[Ti₆O₆[ⁱPrO₆[INA₆]]]}. (b) Coordination environment of the Cu₂I₂ dimer. (c) View of the cage. (d) Crystal photograph of MTM-1.[129] Copyright 2017, RSC.

metal cations and organic linkers undergo self-assembly to form a crystalline metal–organic scaffold. The advantage of the solvent thermal method for preparing MOFs is that the high-temperature, high-pressure environment greatly promotes the solubility and diffusion rate of the reactants, which is conducive to the orderly arrangement of atoms/molecules and crystal growth. Typically, MOF crystals with very high crystallinity and highly ordered structures can be obtained. The products have high specific surface area and porosity. The structure and morphology can be adjusted by controlling the reaction parameters.[129–132] Wang et al.[129] used a solvothermal method to synthesize a three-dimensional (3D) highly crystalline cluster-type Ti-MOF by synergistically assembling hexagonal prismatic {[Ti₆O₆[ⁱPrO₆]]}⁶⁺ clusters and rhombic Cu₂I₂ dimers using isonicotinic acid, as shown in Fig. 5. This demonstrates the high crystallinity of MOFs synthesized *via* the solvothermal method. Liu et al.[130] synthesized a highly crystalline MOF-808 with uniform size and regular structure *via* the solvent method at 130 °C for 5 hours. The resulting MOF material exhibits a specific surface area exceeding 1000 m² g⁻¹ and a pore volume exceeding 0.50 cm³ g⁻¹, along with high thermal stability, as shown in Table 1. Kouser et al.[131] synthesized Zn(INA) microcrystalline MOFs. The structure of the MOFs was confirmed *via* XRD, SEM, and TEM imaging, and their purity was verified through EDS analysis. BET studies indicated that it has a large surface area and pore volume, suggesting potential for various industrial applications. This demonstrates

**Table 1** Specific surface area and pore volume of MOF-808-130 °C synthesized at different times.[130] Copyright 2021

| Sample | BET surface area/(m² g⁻¹) | Pore volume/(cm³ g⁻¹) |
| --- | --- | --- |
| MOF-808-130 °C-1 h | 504 | 0.29 |
| MOF-808-130 °C-5 h | 1004 | 0.53 |
| MOF-808-130 °C-10 h | 1171 | 0.61 |
| MOF-808-130 °C-15 h | 1083 | 0.59 |
| MOF-808-130 °C-20 h | 1232 | 0.68 |

that MOFs synthesized by the solvothermal method have high surface area and high porosity. Hu et al.[132] used hexahydrate nickel chloride (NiCl₂·6H₂O) as the metal salt and terephthalic acid (PTA) as the organic ligand. By altering the type of solvent, they employed a one-step solvothermal method to self-assemble high-loading nickel-based MOF materials (Ni-MOF/NF) on the surface of foam nickel. The better the solvent's solubility for PTA or the higher the pH value, the faster the deprotonation rate of PTA in the solution, and the faster the nucleation rate of the material. The self-grown nickel-based MOF materials exhibit three distinct morphologies—spherical clusters, plate-like, and bulk-under different solvent systems, with corresponding changes in loading capacity. This demonstrates the strong controllability of the solvothermal method.

However, the reaction conditions are harsh, requiring high temperatures (120–200 °C) and high-pressure environments, with equipment dependent on pressure-resistant reactors, posing high operational risks. It is energy-intensive and time-consuming. Reaction times typically range from 6 to 24 hours, and energy consumption does not meet green chemistry requirements. The extensive use of toxic solvents such as DMF not only increases costs and environmental impact but also risks residual solvents blocking pores, necessitating complex post-processing (*e.g.*, ethanol exchange, vacuum drying). Issues such as high temperatures and pressures, prolonged reaction times, extensive solvent use, and potential batch-to-batch variability pose significant challenges when scaling up from laboratory to industrial production.[133–135] As an important method for synthesizing MOF materials, researchers have identified some approaches to address some of these drawbacks, but further exploration of solutions or alternative preparation methods is still needed. For example:

1. The mother liquor-induced synthesis method not only reduces the thermodynamic barriers to crystal nucleation but also induces crystal nucleation and growth, significantly reducing crystallization time while increasing material crystallinity and purity. Professor Jiang Haolong's team successfully induced the synthesis of 100% pure MOFs by pre-synthesizing a small amount of pure-phase zirconium-based MOFs as seeds and adding them to the reaction system, while reducing the reaction time to 1–10 hours.[136]

2. Poor sample reproducibility is primarily due to the failure to accurately control reaction parameters, including reaction time, temperature, pressure, reactant concentration, flow rate, and surface area to volume ratio. Effective control of these parameters ensures catalyst reproducibility.[133]

3. Establishing databases, sharing of open data and the adoption of transparent research practices are capable of substantially improving the reproducibility of studies focused on porous materials.[133]

4. Seeking non-toxic and inexpensive organic solvents or utilizing hydrothermal synthesis instead of solvent thermal synthesis. HKUST-1 was synthesized *via* hydrothermal and solvent thermal methods,[137] with hydrothermal synthesis capable of producing particles with high specific surface area.[134,138,139]

5. Replacing high temperatures with room temperature (RT). The RT synthesis of HKUST-1 (MOF-199) has also been demonstrated by researchers to be scalable. RT synthesis involves mixing the copper acetate metal precursor with a pre-homogenized aqueous suspension of $H_3BTC$ for one hour to achieve a space-time yield (STY) of 2035 kg m$^3$ day$^{-1}$. Typically, RT synthesis requires pre-activating ligands using salt-like ligands or by adding a base to deprotonate the ligands, as this promotes faster nucleation during synthesis. In terms of surface area and crystallinity, the properties of MOFs synthesized by this method are comparable to those of traditional and industrial syntheses. Although RT synthesis can be easily scaled up for production and offers higher yields and lower energy consumption compared to current industrial production of HKUST-1, the limitations of using deprotonated ligands for MOF synthesis significantly restrict the flexibility of RT synthesis.[140–143]

### 4.4. Calcination

Calcination for the preparation of MOF photoelectrocatalytic materials is a method of treating MOF materials at high temperatures in order to change their physical and chemical properties and thus improve their photoelectrocatalytic properties. The calcination process removes impurities and volatiles from the MOF materials and improves their thermal and chemical stability. The calcined MOF materials have higher stability and catalytic activity, and can be applied in a wider range of fields, such as environmental pollution control, energy conversion, and organic synthesis, *etc.* Pan *et al.*[144] employed a two-step calcination process to convert ZIF-8 for the preparation of porous carbon (C). As illustrated in Fig. 6, the resulting modified structure successfully incorporates C doping into the ZnO lattice while preserving its cubic morphology. Li *et al.*[145] were the first to demonstrate that core–shell heterojunctions



**Fig. 6** Schematic illustration of the fabrication of the ZnO@M@-ZIF-67 photoanode for PEC water splitting.[144] Copyright 2016, Elsevier.

derived from MOFs exhibit enhanced photoelectrochemical (PEC) water splitting efficiency. The photovoltaic electrodes were prepared by coating MOF $NH_2$-MIL-125 (Ti) onto $Fe_2O_3$ nanorods using a solvothermal procedure and subsequent two-step calcination to form $Ti_xFe_{1-x}O_y$ shell/$Fe_2O_3$ core nanorod arrays. However, the calcination method may lead to structural damage, which may collapse the structure of the MOF material or decompose the organic ligands, affecting its catalytic performance. The calcination process consumes a lot of energy and time, which increases the preparation cost. In addition, the use and maintenance of the calcination equipment also require a certain cost investment. Limited material selectivity and the limited variety of MOF materials currently available for the calcination method may limit their application in some specific areas.

### 4.5. Mechanochemical method

Mechanochemical synthesis involves grinding metal salts and organic ligands to prepare MOFs. Molecular bonds are disrupted by mechanical forces during milling, leading to the formation of new products through re-coordination. The first study of mechanochemical synthesis of MOFs was reported by Pichon *et al.*[146] in 2006. The process involves no solvent and the target product can be synthesized within 10 minutes under mild conditions, offering time efficiency but yielding products with low purity and poor crystallinity. To address these limitations, researchers have modified the protocol by introducing a liquid-assisted grinding (LAG) approach. Specifically, Friščić's group[147] incorporated a minimal amount of solvent during the milling stage, leveraging the liquid's structural-directing effects to enhance reaction kinetics and crystal quality (Fig. 7). Despite the advantages of high synthesis efficiency and reduced solvent usage in mechanochemical methods, the resulting MOFs often exhibit suboptimal crystallinity and impurity inclusion.[148]

### 4.6. Ultrasonic method

Sonochemical synthesis, in simple terms, is a synthetic process that harnesses ultrasound-generated energy to regulate chemical reactions. Among the various methods for the synthesis of MOFs, the ultrasonic method is an economical and eco-friendly method, which can provide high yields under mild operating conditions. Yang *et al.*[149] used an ultrasound-assisted method to uniformly coat an ultrathin CoFe MOF layer on the surface of a $BiVO_4$ photoanode to construct a type II heterojunction and to promote charge separation and transfer. The optimized photoanode achieved a photocurrent density of 3.92 mA cm$^{-2}$ at 1.23 V *vs.* RHE and a photonic current efficiency (IPCE) of 89% at 400 nm, as shown in Fig. 8. However, the reactivity of this method exhibits limited controllability, often leading to the emergence of parasitic reactions and the incorporation of impurities within the synthesized products.

### 4.7. Microwave method

The microwave method was first reported in 2005.[150–152] As an emerging material synthesis technique, it has been widely used for the preparation of MOFs in recent years. Its main
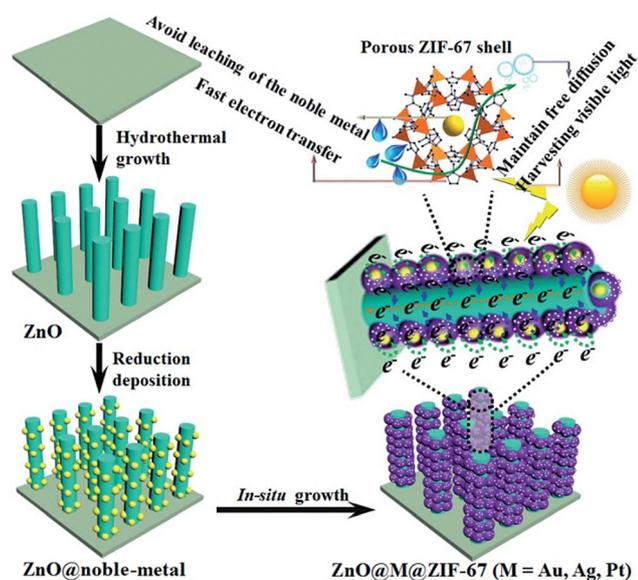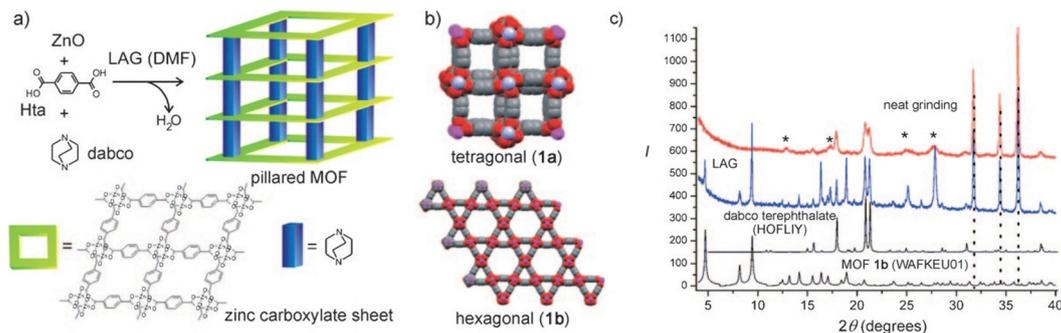
Fig. 7 (a) Expected MOF 1 assembly; (b) MOF isomers 1 a and 1 b; red O, gray C, blue N, purple Zn. (c) PXRD patterns (top to bottom): 60 min neat grinding (red; no reaction), 60 min LAG (blue; partial reaction), simulated pattern for the dabco-Hta salt and for 1 b (in square-root scale). Dotted lines indicate reflections of ZnO; reflections of residual Hta are labeled "☆".[147] Copyright 2010, Wiley.
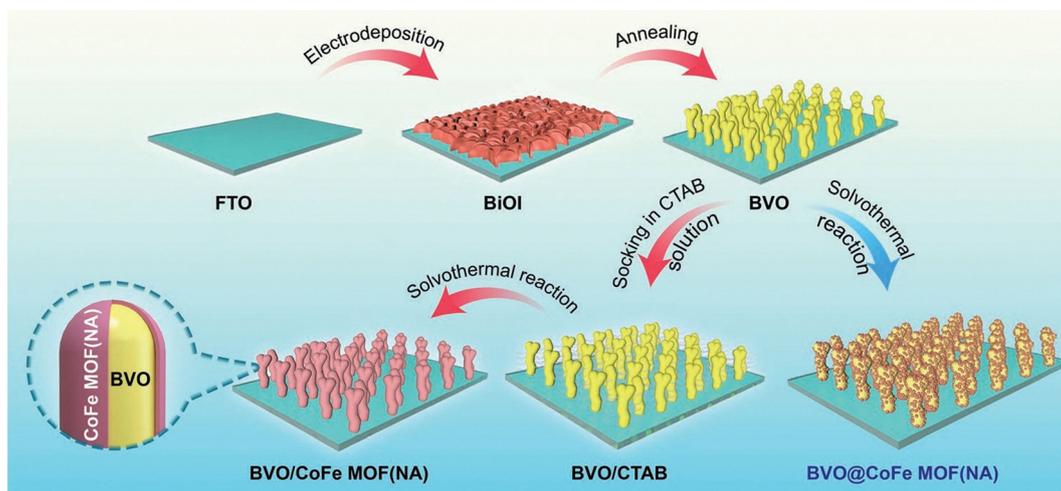


Fig. 8 Schematic illustration of the synthesis process of BVO/CoFe MOF(NA) and BVO@CoFe MOF(NA) photoanodes.[149] Copyright 2023, Wiley.

working principle is based on the unique mechanism of microwave–matter interaction, which promotes intermolecular coordination reactions of reactants through rapid and uniform heating, thus realizing efficient synthesis. MIL-125(Cr) represents the initial MOF synthesized through microwave-assisted methods, exhibiting a 44% yield after 4 hours at 220 °C. In contrast, conventional heating methods required 4 days to attain a comparable yield.[153] Wu et al.[154] used a microwave-assisted synthesis method to prepare soluble porphyrin MOFs (Al-PMOF), as shown in Fig. 9. Since Al-PMOF itself does not possess active sites for water splitting to produce hydrogen, $(Pd(CH_3CN)_2Cl_2)$ was introduced as a precursor for Pd. Pd nanoparticles were deposited onto Al-PMOF via photodeposition, enabling the use of Pd nanoparticles as co-catalysts in photocatalytic water splitting experiments. The microwave method significantly reduced reaction time (30 minutes at 140 °C, compared to 16 hours at 180 °C using traditional methods). Compared to bulk MOF (Bulk-Al-PMOF), the photocatalytic water splitting activity for hydrogen production was enhanced by 14 times. The synthesis of MOFs using microwave irradiation can effectively decrease reaction times and enhance the crystal quality of MOFs. Moreover, this method
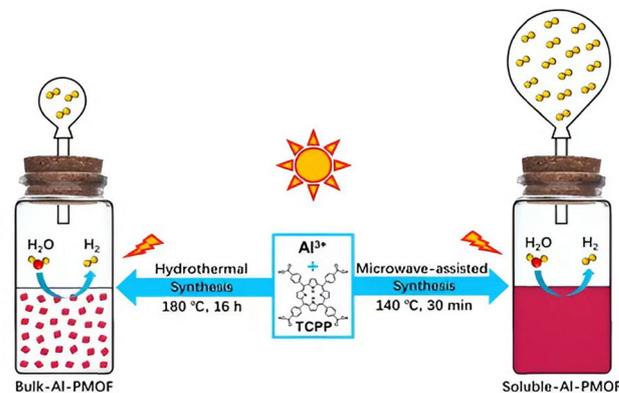


Fig. 9 Schematic illustration of the synthesis process of S-Al-PMOF.[154]

embodies environmentally friendly practices, energy efficiency, and operational simplicity. Nonetheless, it is essential to acknowledge that this approach necessitates precise instrumentation for regulating microwave energy and mandates that metal ions possess strong electromagnetic wave absorption capabilities, thereby somewhat constraining its applicability.

**Table 2** Synthesis methods of MOFs and their derivatives as photocatalysts

| Synthesis method | Advantages | Disadvantages |
|---|---|---|
| Sedimentation | 1. High controllability | 1. May have substrate requirements<br>2. May increase process complexity |
| In situ growth method | 1. High controllability<br>2. High stability<br>3. Simple preparation process<br>4. No complex equipment required<br>5. Easy to operate | 1. Reaction conditions must be precisely controlled<br>2. Material selection is limited<br>3. Yields may be low |
| Solvothermal | 1. No special equipment required<br>2. Crystals can be grown | 1. Long synthesis time<br>2. Low yield; difficult to produce on a large scale |
| Calcination | 1. Improve thermal stability and chemical stability<br>2. Enhance catalytic activity<br>3. Applicable to a wider range of fields | 1. Requires a significant amount of energy and time<br>2. The use and maintenance of calcination equipment incurs costs<br>3. Material selection is limited |
| Mechanochemical method | 1. No solvents involved<br>2. Mild reaction<br>3. Time-saving | 1. The product has low purity and poor crystal form |
| Ultrasonic method | 1. Low cost<br>2. Environmentally friendly<br>3. Mild operating conditions | 1. The reaction is difficult to control<br>2. May be accompanied by side effects |
| Microwave method | 1. Highly efficient synthesis | 1. Microwave energy is difficult to control<br>2. Metal ions must have good electromagnetic wave absorption capacity<br>3. Weak universality |

Table 2 summarizes the advantages and disadvantages of various methods.

# 5. Performance optimization strategies

Since the photoelectrocatalytic water splitting mechanism was mentioned earlier, the steps of photoelectrocatalysis are divided into light absorption to produce carriers, carrier separation, and surface chemical reaction. Therefore, the performance of photoelectrode materials is limited by several energy loss mechanisms as follows: (1) when the incident photon energy exceeds the semiconductor band gap, the excess energy is dissipated as heat or photoluminescence, resulting in a low utilization of light energy. (2) Energy band structure mismatch and poor conductivity can hinder carrier separation, leading to lower catalytic efficiency. (3) Photogenerated carriers may be complexed in the bulk phase or on the surface, resulting in fewer carriers effectively participating in the reaction. (4) HER/OER at high energy barriers may result in carrier depletion while simultaneously inducing electrode polarization or material corrosion. To optimize their performance, ideal photoelectrode materials should be developed through three key strategies: enhancing light absorption, modulating carrier dynamics, and engineering surface reactions. These approaches are essential for achieving efficient conversion of solar energy into hydrogen.

The bandgap ($E_g$) of MOFs directly determines their light absorption range, and narrow bandgap MOF materials can utilize visible light or even near-infrared light. Therefore, it is feasible to reduce the bandgap of MOFs by modifying them and developing new MOFs. Moreover, the efficiency of photogenerated charge carrier (electrons and holes) migration is a critical determinant of photoelectrode performance. The construction of rational heterostructures of MOFs together with other semiconductor materials is the key to promote charge separation. Surface electrochemical reactions constitute the final and rate-determining step in photoelectrochemical water splitting. The surface properties of photoelectrode materials critically govern the efficiency of charge carrier utilization. Specifically, surface defects, dislocations, and active sites act as reaction centers where photogenerated electrons and holes participate in redox reactions. However, these defects can either enhance or impede catalytic performance depending on their type, density, and distribution.[62,155] The direct contact of electrolytes with the photoelectrode and the attachment of $H_2/O_2$ bubbles are the two key factors leading to the deterioration of the surface electrochemical reaction. The former destroys the material structure through chemical/photocorrosion mechanisms, and the latter exacerbates the reaction inhomogeneity through physical hindrance and local potential fluctuations. Moreover, for long-term photoelectrocatalytic reactions, the stability of the photoelectrode material must be high, as shown in Fig. 10. Therefore, further improving the stability of MOFs is also an important research direction. Future research will focus on designing and optimizing the photoelectrocatalytic materials, investigating the energy band structure, surface state and carrier transport mechanism of the photoelectrocatalytic
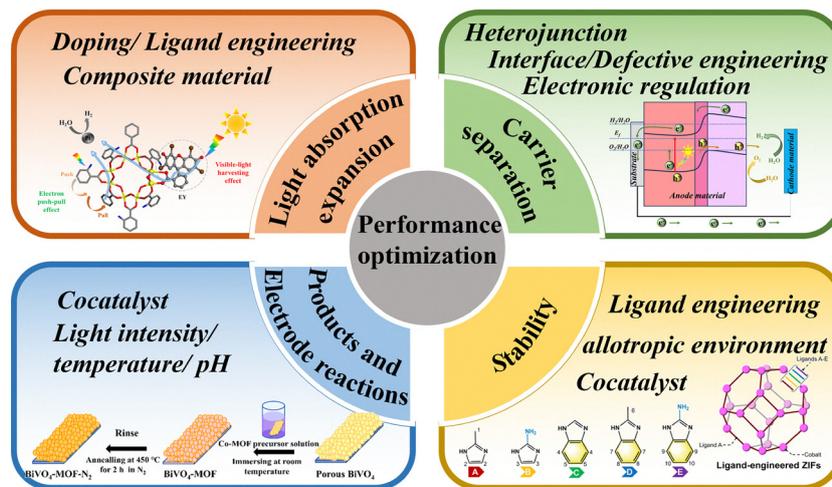
**Fig. 10** Performance optimization strategies for photoelectrocatalytic water splitting materials.

materials, and improving the photoelectrocatalytic activity, light absorption performance, carrier mobility and stability of the photoelectrocatalytic materials through structural design of the materials, component modulation and doping modification.

### 5.1. Light absorption extension and energy level structure

Light absorption in photoelectrocatalysts refers to the process of photon interaction with the material, which determines the onset of light excitation, affects charge separation and migration, and is a key step in applications such as hydrogen production by photoelectrocatalysis. The light absorption efficiency is a measure of the photocatalyst's ability to absorb light. In photoelectrocatalysis, carrier production is directly related to the material's bandgap width and absorption coefficient, and increasing the light absorption efficiency is essential to increase the production of electron–hole pairs.[156] The bandgap width determines the light absorption capacity of the photoelectrode material throughout the solar spectrum, thereby establishing the material's maximum potential efficiency for solar-to-hydrogen (STH) conversion. Heterojunction materials featuring a narrow bandgap structure exhibit enhanced light absorption within the solar spectrum. However, the bandgap cannot be excessively narrow as it must still supply an ample driving force for both the oxygen and hydrogen precipitation reactions.[157] The energy band structure of a photoelectrocatalytic material is an important property that determines the energy state

of the photoexcited carriers. Photoelectrodes for PEC water splitting devices must meet specific criteria regarding their energy band positions, including appropriate band gap, valence band, and conduction band levels. It is essential for the conduction band edge of these materials to be positioned lower than the water reduction potential $E$ ($H^+/H_2$), while the valence band edge should be situated above the oxygen reduction potential $E$ ($O_2/H_2O$). Semiconductor materials are ideal for PEC photoelectrodes because of their tunable energy band edge positions and bandgap widths. To achieve optimal performance, these semiconductors must efficiently utilize most of the visible light spectrum and maintain stability under dim light conditions in order to use sunlight to decompose water into commercially viable hydrogen. Optimizing the energy band structure is key to improving photoelectrocatalytic performance. Researchers have explored various material modification methods such as elemental doping, composites and ligand functionalization to further improve the performance. Table 3 briefly describes the extended photoabsorption catalytic materials reported in recent years for PEC water cracking.

**5.1.1. Element doping.** Doping impurity elements can modify the band gap by introducing impurity energy levels within the band gap or by creating solid solutions to broaden the semiconductor's width, thereby expanding its light absorption spectrum. Therefore, the electronic structure of MOFs can be altered by introducing heteroatoms to narrow

**Table 3** Some of the recently reported materials with extended photoabsorption and their properties for PEC water cracking

| Photoelectrode | Modification method | $H_2$ evolution rate | Light absorption range | Bandgap energies | Photocurrent density *vs.* RHE | Ref. |
|---|---|---|---|---|---|---|
| CuSL–CuBr | Heteroatom doping | 50.28 mmol g$^{-1}$ h$^{-1}$ | 250–600 nm | 2.30 eV | 0.64 μA cm$^{-2}$ | 158 |
| Mn-FeBTC/NIF | Heteroatom doping | — | 380–800 nm | 1.53 eV | — | 159 |
| Cu$_3$HHAE$_2$ | Composite material | — | up to 1600 nm | 0.87 | 260 μA cm$^{-2}$ (0.1 M Na$_2$SO$_4$ 0 V) | 160 |
| Ag/Au HPNS-Cd$_{0.8}$Zn$_{0.2}$S NSs | Composite material | — | 365–850 nm | 1.7 eV | 0.16 mA cm$^{-2}$ (0.65 V) | 161 |
| Co$_3$C$_{-x}$/TiO$_2$ | Ligand functionalization | — | 390–850 nm | 1.42 eV | 2.6 mA cm$^{-2}$ (1 M NaOH 1.23 V) | 163 |
| Ti$_6$((μ$_3$-O)$_2$(Oi-Pr)$_8$) (LA)$_2$·i-PrOH (S1) | Ligand functionalization | — | 200–510 nm | 2.85 eV | 2. 12 μA cm$^{-2}$ (0.2 M Na$_2$SO$_4$) | 165 |

the band gap or introduce intermediate energy levels to extend the light absorption range into the visible or even near-infrared region. Lin et al.[158] proposed an atomically precise heterogeneous cluster assembly strategy to construct two isostructured three-dimensional MOF materials, CuSL–CuX (X = Cl, Br) with a cds topological network. The CuSL–CuX material integrates hexanuclear copper–sulfur clusters $Cu_6S_6$ and binuclear copper–halogen clusters $Cu_2X_2$, which not only endows the material with excellent stability over a wide pH range (1–14) (Fig. 11a), but also achieves broad-spectrum visible light absorption (Fig. 11c). The CBM positions of CuSL–CuBr and CuSL–CuCl can be estimated to be −0.75 and −0.79 V, respectively (Fig. 11f), both of which are more negative than that of the potential for the reduction of $H^+$ to $H_2$, satisfying the thermodynamic requirements for photocatalytic water splitting. Thus, CuSL–CuBr and CuSL–CuCl show potential as effective materials for efficient photocatalytic $H_2$ production under visible light exposure, emphasizing the effectiveness of the heterogeneous cluster self-assembly strategy in developing highly stable MOFs.

Dong et al.[159] deposited the semiconductor Mn-FeBTC on a well-conducting nickel iron foam and used a trace Mn doping strategy to efficiently modulate the BIEF of the Mott Schottky heterojunction formed by FeBTC and a metal substrate. The Mn-FeBTC/NIF composite exhibited enhanced light absorption across the 380–800 nm range, peaking at 68.5% at 738 nm. Additionally, there was a 0.28% increase in maximum absorption intensity at 597 nm, which is due to the increase in photosensitivity caused by the decrease in band gap due to Mn doping.

**5.1.2. Composite materials.** Composite materials are compounds composed of two or more materials. Through the synergistic action of multiple components, their energy band structure can be adjusted and their light absorption range expanded. In view of this, Dong et al.[160] reported a layered conductive conjugated MOF material containing an aryl-ethynylidene-type subethynylidene sp-coordinated macrocyclic ligand structure bonded to $CuO_4$, which was named $Cu_3HHAE_2$. 2D-MOFs with sp carbon atoms exhibit semiconducting behaviors and a wide optical absorption interval (the optical absorption interval up to 1600 nm in the near-infrared (NIR)), as shown in Fig. 12c. Due to the presence of abundant acetylene structures, this MOF was first used as a MOF photoelectrode for the photoelectrocatalytic production of hydrogen, and a current density of 260 μA cm$^{-2}$ was achieved at an overpotential of 0 V vs. RHE. Li et al.[161] prepared a new type of MOF using a metal–organic framework material (ZIF-8) as a template through a multi-step derivatization and in situ embedded synthesis technique. Synthesis technique to prepare a novel plasma-enhanced catalyst (Ag/Au HPNS-$Cd_{0.8}Zn_{0.2}$S NSs). It was found that the (Ag/Au HPNS-$Cd_{0.8}Zn_{0.2}$S NSs) was able to extend the light absorption range of intrinsic ZIF-8 from the ultraviolet region to the near-infrared region due to the good light absorption properties of $Cd_{0.8}Zn_{0.2}$S and the photosensitization effect of Ag/Au HPNS. However, there are many drawbacks to this approach; first, the complexity of the composite structure of the materials often leads to difficulties in controlling the distribution and interactions of the active components, resulting in inconsistent performance; second, due to the use of multiple components, the cost of preparation tends to be high; in addition, the stability of these materials under long-term photoelectrocatalytic operation remains a challenge. Finally, optimization of composition and structure for specific applications requires significant research efforts.
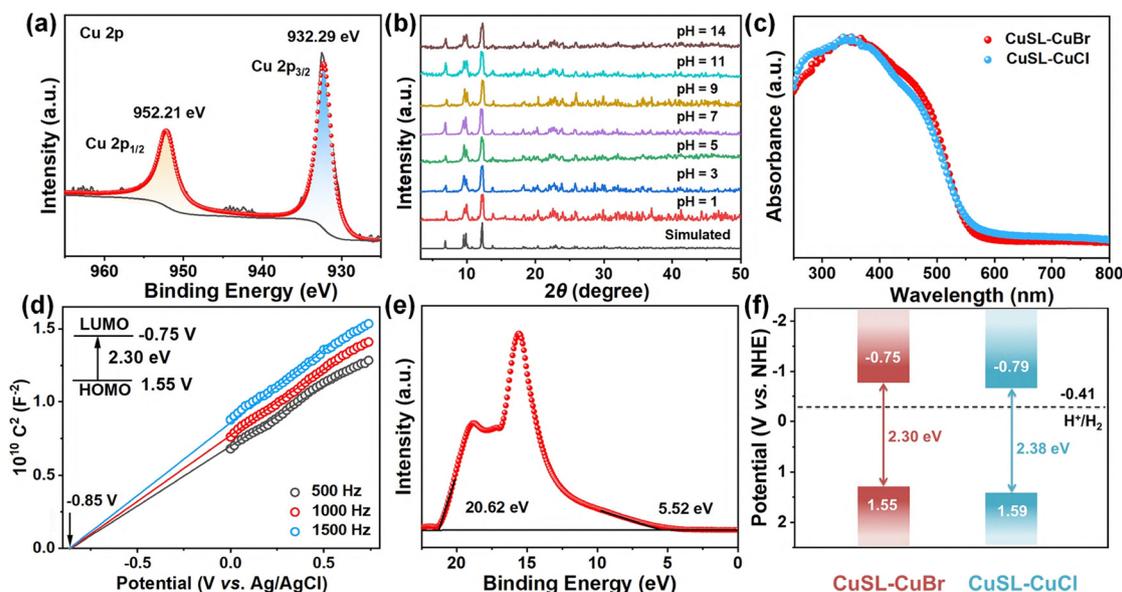


Fig. 11 (a) Cu 2p XPS spectrum of CuSL–CuBr. (b) PXRD patterns of CuSL–CuBr after immersion in solutions of varying pH for one week. (c) UV-vis diffuse reflectance spectrum of CuSL–CuBr and CuSL–CuCl. (d) Mott–Schottky plot of CuSL–CuBr. (e) UPS spectra of CuSL–CuBr. (f) Band structure diagram of CuSL–CuBr and CuSL–CuCl.[158] Copyright 2025, Wiley.
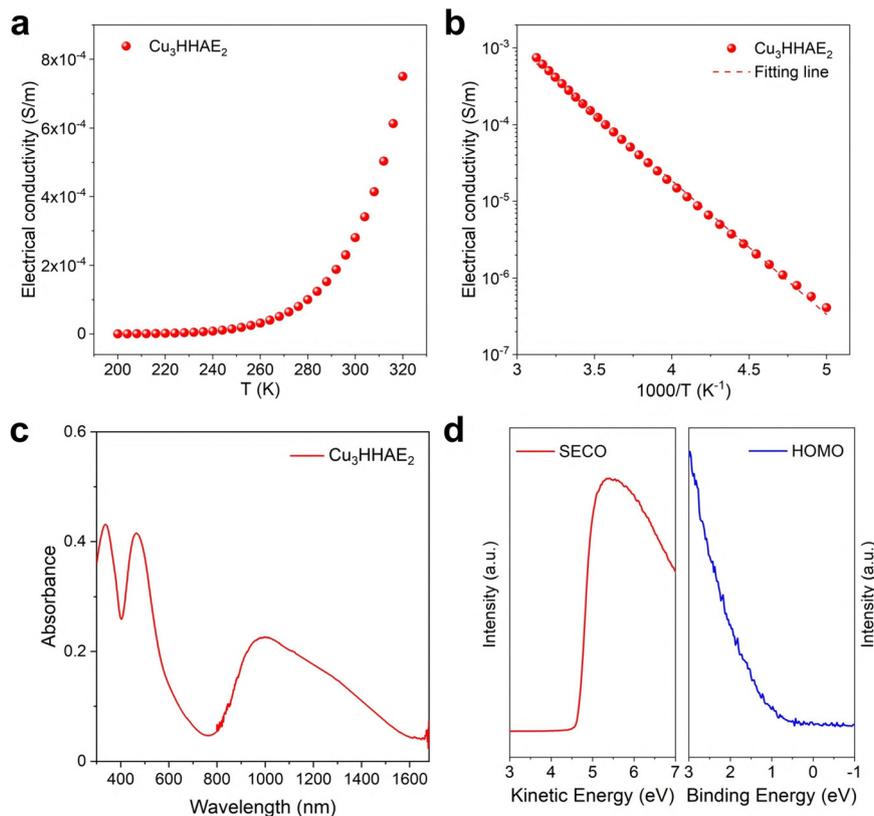
Fig. 12 (a and b) Variable-temperature electrical conductivities of $Cu_3HHAE_2$. (c) Vis-NIR absorption spectroscopy of $Cu_3HHAE_2$. (d) UPS results of $Cu_3HHAE_2$; the left image is the low kinetic energy region of the UPS spectra, and the right image is the low binding energy region (HOMO).[160] Copyright 2022, Wiley.

**5.1.3. Regulating organic ligand/ligand functionalization.** By tuning the organic ligands, the electronic structures and energy band gaps of MOF materials are altered to extend the light absorption range. In addition, the light absorption properties and PEC water splitting performance of MOFs can be further improved by introducing visible light responsive units and functional features.[162] Yi *et al.*[163] utilized MOF-derived narrow bandgap $Co_3C$ nanosheets coupled with hollow $TiO_2$ nanocages to form a heterojunction photoanode. The narrow

bandgap property of $Co_3C$ extends the light absorption range, while the type-II heterojunction reduces carrier complexation, and the photocurrent density reaches 2.6 mA cm$^{-2}$ (1.23 V), which is higher than that of pure $TiO_2$ by 201%, as shown in Fig. 13a. Coupling $TiO_2$ with $Co_3C$, the optical absorption of $Co_3C_{-x}/TiO_2$ was greatly enhanced in the visible range, and this result confirms that coupling $Co_3C$ with $TiO_2$, which has a narrow bandgap energy, can effectively broaden the optical trapping range of $TiO_2$.
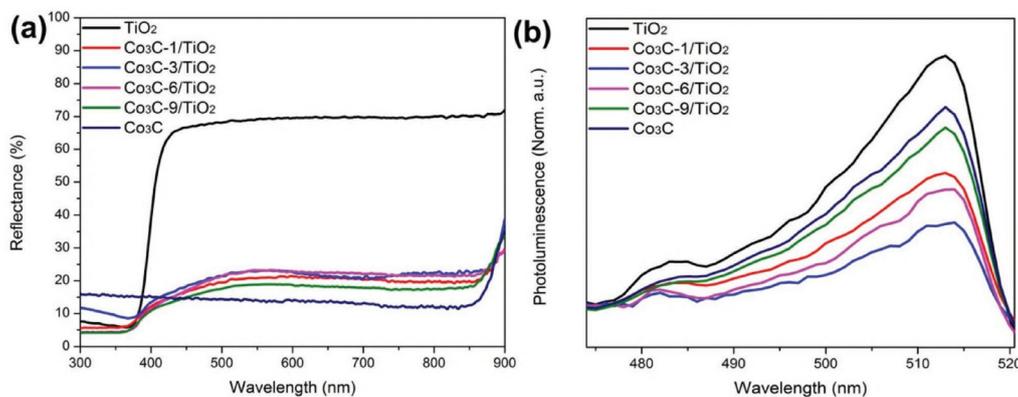


Fig. 13 (a) UV-vis DRS spectra and (b) normalized photoluminescence spectroscopy of $TiO_2$, $Co_3C_{-x}/TiO_2$ ($x$ = 1, 3, 6, 9) and $Co_3C$.[163] Copyright 2018, Wiley.
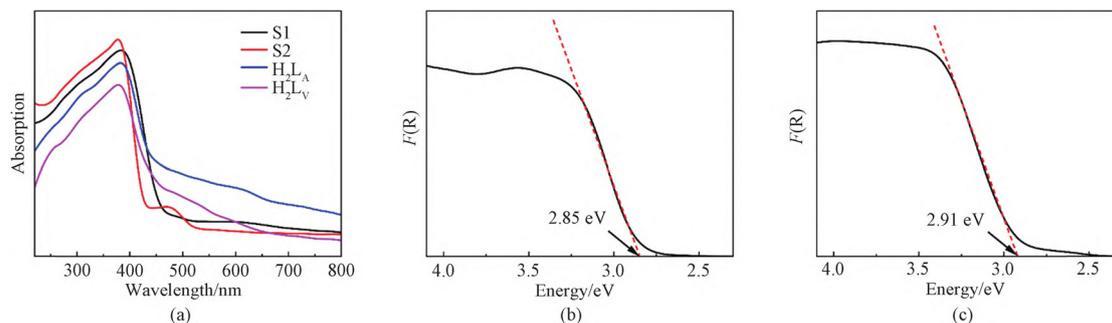
**Fig. 14** Solid-state UV-vis spectra and band gap: (a) absorption spectra of S1, S2 and ligands; (b) and (c) Kubelka−Munk transformation of diffuse reflectance data of S1 and S2.[165]

Hu et al.[164] first modified the –NH$_2$ group onto MIL-125 using a ligand functionalization strategy to obtain NH$_2$-MIL-125, and then successfully prepared Cu–NH$_2$-MIL-125 by Cu ion coordination. This dual modification strategy resulted in a reduced band gap and a wider range of light absorption, exhibiting excellent piezoelectric–photocatalytic activity (2884.2 μmol g$^{-1}$ h$^{-1}$). In addition, by introducing chromophores or photosensitizers with strong light-absorbing ability, the light-absorbing ability of the MOF materials can be enhanced and their photoresponsive range can be extended to the visible region. Yang et al.[165] utilized naphthalene diimide (NDI) ligands, H$_2$LA, as photo-active sensitizing molecules, and designed and synthesized the cyclic titanium–oxygen clusters Ti$_6$((μ$_3$-O)$_2$(Oi-Pr)$_8$)(LA)$_2$·i-PrOH (S1). As shown by ultraviolet-visible (UV-vis) spectroscopy and photocurrent tests, the NDI ligand not only extended the absorption edge of S1 to 500 nm, but also caused S1 to display a photocurrent density as high as 2.12 μA cm$^{-2}$, thus demonstrating the importance of the photoreactive ligand in the modulation of the photoresponse of TOCs, as shown in Fig. 14.

## 5.2. Photogenerated charge transport and utilization

The efficiency of photocatalytic reactions is directly dependent on the effective separation of photogenerated electrons and holes. During photocatalysis, electron–hole pairs are generated by the absorption of light energy by the semiconductor material, but if these carriers are compounded before migrating to the surface to participate in the reaction, it will lead to energy waste and reduce the overall efficiency. For example, studies of Al-doped SrTiO$_3$ have shown[166] that by suppressing carrier complexation and optimizing the charge separation mechanism, the quantum efficiency can be close to 100%, and high efficiency water splitting can be achieved even with extremely short carrier lifetimes (sub-nanosecond). Optimizing charge separation also enhances the photocurrent density. The carrier separation efficiency directly affects the rate of redox reaction on the surface of the photoelectrode. For example, atomic layer mesoporous In$_2$O$_{3-x}$/In$_2$S$_3$ heterojunction[167] shortens the carrier migration distance through interfacial strong coupling and mesoporous structure, and achieves a photocurrent density of 1.28 mA cm$^{-2}$ (1.23 V vs. RHE), which is significantly higher than that of a single material. Some materials are limited in their light absorption or charge transport ability due to bandgap or defect issues, which need to be optimized by carrier separation strategies. For example, Sn-doped SrTiO$_3$ suppresses Ti$^{3+}$ defects (carrier complex centers) by replacing Sr sites[168] with Sn$^{2+}$ to improve the overall water splitting efficiency by a factor of 10.4. Enhancing the carrier separation efficiency is the key to the practicalization of photoelectrocatalytic water splitting technology. Therefore, future studies of photoelectrocatalytic MOF materials need to further explore the carrier separation mechanism with low energy consumption and high stability to promote the large-scale application of green hydrogen energy. Table 4 briefly describes the catalytic materials that have been reported in recent years to enhance carrier separation efficiency for PEC water cracking.

**5.2.1. Heterogeneous structure construction.** Heterojunction structures represent a highly promising and efficient catalytic strategy. Its core mechanism lies in the formation of an intrinsic electric field at the interface, which can accelerate the directional separation and migration of photogenerated carriers, thereby laying a crucial foundation for enhancing catalytic performance. Therefore, the design and construction of heterojunction structures by combining metal–organic frameworks (MOFs) with semiconductor materials through rational design has emerged as an effective solution. This structural design enhances charge separation efficiency by optimizing charge separation and transport pathways, ultimately providing robust support for the enhancement of photocatalytic hydrogen production performance. Yang et al.[149] designed and synthesized a BiVO$_4$/CoFe MOF heterojunction structure to promote charge transfer for efficient photoelectrochemical splitting of water. An ultrathin bimetallic CoFe MOF layer was modified on the BVO photoanode to construct a high-quality charge–transfer interface, which was used to realize efficient charge separation and transfer. The optimized BVO/CoFe MOF(NA) photoanode achieves a photocurrent density of 3.92 mA cm$^{-2}$ at 1.23 VRHE, which is 6.03 times higher than that of the pristine BVO. Femtosecond transient absorption (fs-TA) spectroscopy characterizing the ultrafast charge transfer process of BVO/CoFe MOF(NA) exhibits a positive PA signal with an initial accumulation time of about 0.44 ± 0.09 ps, which is much faster than that of BVO (1.77 ps), as shown in Fig. 15. The reason for this phenomenon may be that the introduction of CoFe MOF(NA)

**Table 4** Some recently reported materials for enhancing carrier separation efficiency and their performance for PEC water cracking

| Photoelectrode | Modification method | Charge recombination lifetime | Faradaic efficiency | Photocurrent density 1.23 V vs. RHE | Ref. |
|---|---|---|---|---|---|
| $BiVO_4$/CoFe MOF | Heterojunction | 89 ns | 92% | 3.92 mA cm$^{-2}$ (1 M KBi) | 149 |
| Co-agZIF-62/NiO/$BiVO_4$ | Interface engineering | 22.12 ns | — | 5.34 MA cm$^{-2}$ | 169 |
| NiCo-MOFCuCrO$_2$-$BiVO_4$ | Interface engineering | — | 95.3% | 5.75 mA cm$^{-2}$ | 170 |
| Ov-$BiVO_4$/MIL-101 | Defective engineering | 6.62 ns | — | 5.91 mA cm$^{-2}$ (1 M KBi pH = 9) | 171 |
| Vw-$WO_3$ | Defective engineering | 13.61 | Nearly 1 | 4.0 mA cm$^{-2}$ ($Na_2SO_4$ pH = 7) | 172 |
| $Co_3O_4$/CoV-MOF/$BiVO_4$ | Defective engineering | 10 ns | | 6.0 mA cm$^{-2}$ | 173 |
| (Co, Ni)-MOF/$WO_3$/W | Electronic control | — | 90.07% | 2.96 mA cm$^{-2}$ (0.5 M $Na_2SO_4$) | 174 |
| $BiVO_4$ @aNiFc-MOFs | Electronic control | 35.31 ns | 92.1% | 4.34 mA cm$^{-2}$ (0.5 M KBi) | 175 |
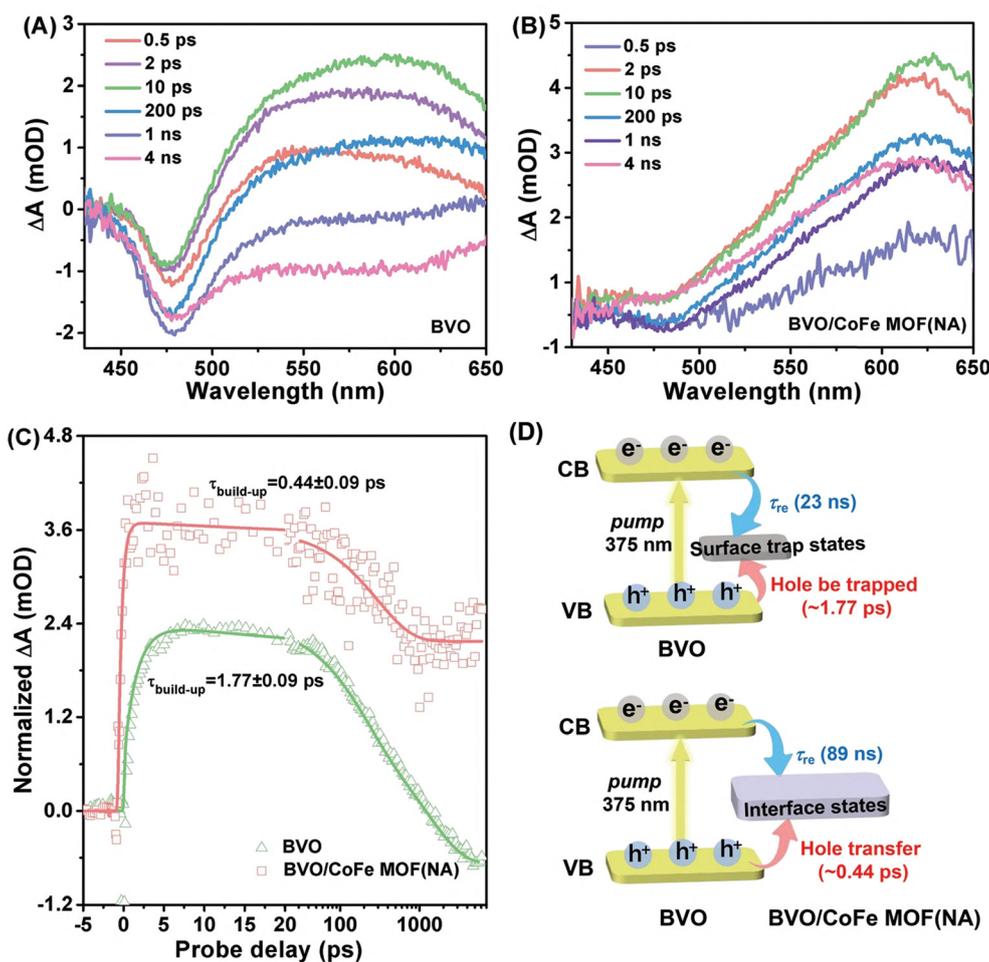


**Fig. 15** Femtosecond transient absorption (fs-TA) spectra of (A) BVO and (B) BVO/CoFe MOF(NA) excited at 375 nm. (C) Normalized fs-TA spectra probed at 620 nm for the BVO and BVO/CoFe MOF(NA) under 375 nm excitation. (D) Electron transfer pathways involved in BVO and BVO/CoFe MOF(NA) heterostructure systems. τre represents charge recombination lifetime.[149] Copyright 2023, Wiley.

effectively closes the hole-transfer channel in the valence band of BVO to its surface trap state, revealing the transfer of photo-generated holes in the valence band of BVO to the neighboring MOF interface states, which significantly enhances the separation efficiency of the electron–hole pairs in the heterostructure of the BVO/CoFe MOF(NA).

**5.2.2. Interface engineering.** Interfacial engineering refers to the optimization of interfacial structure, electronic state, charge distribution and reaction kinetics by modulating the

physicochemical properties of material interfaces, so as to enhance the performance of materials in the fields of photoelectrocatalysis, photovoltaic conversion and energy storage. The core objective is to achieve efficient carrier separation and transport, optimization of reactive active sites and stability enhancement through interfacial modulation, and ultimately to break through the bottleneck of the intrinsic performance of materials. Song and colleagues[169] developed an integrated Co-agZIF-62/NiO/MO (metal oxide: $Fe_2O_3$, $WO_3$ and $BiVO_4$)
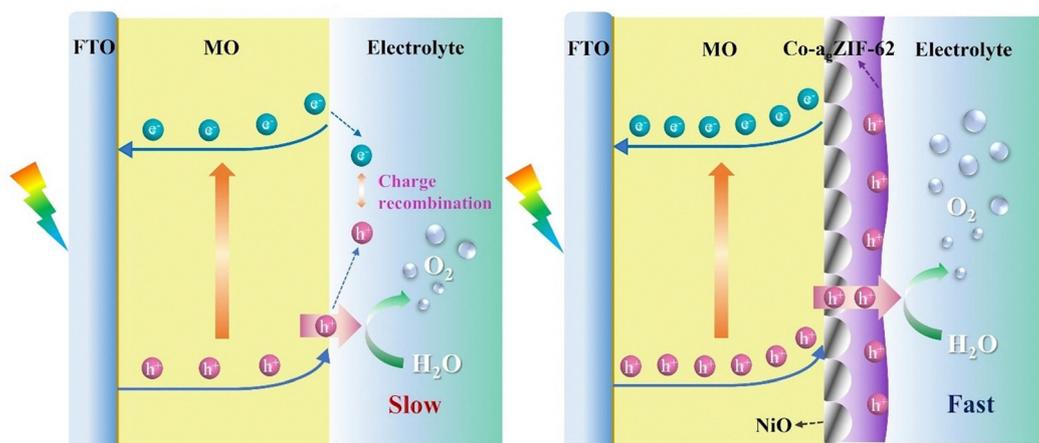
**Fig. 16** A schematic illustration of the charge transfer process on MO and Co-agZIF-62/NiO/MO photoanodes.[169] Copyright 2023, Wiley.

photoanode. The Co-agZIF-62/NiO/BiVO$_4$ photoanode demonstrated a photocurrent density of 5.34 mA cm$^{-2}$ at 1.23 VRHE, exhibiting significantly improved photocurrent stability. This enhancement can be attributed to the incorporation of a NiO hole-transporting layer, which facilitates the establishment of a charge transfer pathway between the BiVO$_4$ substrate and the Co-agZIF-62 catalyst layer. This pathway enables rapid charge transfer to the Co-agZIF-62 layer for the photoelectrochemical (PEC) water oxidation reaction, effectively mitigating charge recombination, as depicted in Fig. 16.

Tian et al.[123] used an interface engineering-assisted energy level modulation strategy to effectively optimize the photocatalytic water oxidation performance of bismuth vanadate photoanodes. The coupling of the CuCrO$_2$ HTL (hole transport layer) with the BiVO$_4$ photoanode generated an in-built electric field, which efficiently facilitated the interfacial migration of carriers. In addition, the in situ growth of NiCo-MOF exhibits a dual effect. On the one hand, the specific functional groups present in NiCo-MOF can effectively passivate the surface defect states of the BiVO$_4$ photoanode, thus significantly reducing the surface recombination of carriers. On the other hand, in NiCo-MOF, the bimetallic elements Ni and Co as OER active sites can

significantly accelerate the kinetic process of the water oxidation reaction. Under the synergistic effect of the CuCrO$_2$ HTL and further in situ growth of NiCo-MOF, the photogenerated holes can migrate to the semiconductor/electrolyte interface rapidly and participate in the water oxidation reaction in time, which greatly enhances the water oxidation performance of the PEC of the BiVO$_4$ photoanode, as shown in Fig. 17.

### 5.2.3. Defective engineering

Defect engineering is also an effective method to enhance carrier separation efficiency. Defect engineering significantly enhances the carrier separation efficiency of MOF catalysts in PEC water splitting through electronic structure modulation, surface property optimization, and carrier dynamics enhancement (the pores or interfaces formed by the defects promote the reactant diffusion and electron transfer).[170] Xin et al.[171] proposed a molecular epitaxial growth technique based on oxygen vacancy (Ov)-driven molecular epitaxial growth on the BiVO$_4$ surface to prepare a uniform MIL-101 layer (Ov-BiVO$_4$/MIL-101 composite structure). This technique generates a high concentration of oxygen vacancies on the BiVO$_4$ surface by electrochemical etching, which promotes the molecular-level
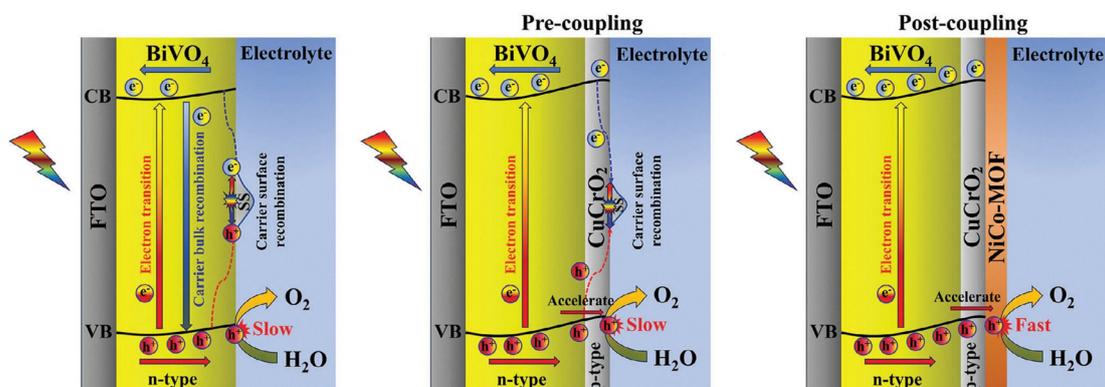


**Fig. 17** Working mechanism diagram of the BiVO$_4$ photoanode, CuCrO$_2$–BiVO$_4$ photoanode and NiCo-MOF–CuCrO$_2$–BiVO$_4$ photoanode.[123] Copyright 2025, Wiley.

binding of MIL-101 to $BiVO_4$ and significantly improves the interfacial charge separation and transport efficiency. The photocurrent density of the Ov-$BiVO_4$/MIL-101 composite photoelectrode reaches 5.91 mA cm$^{-2}$ at 1.23 VRHE potential, which is 2.93 times higher than that of the conventional $BiVO_4$, and achieves a 4.33% in the unbiased solar-hydrogen conversion system with a solar-hydrogen efficiency. Wang et al.[172] proposed an innovative strategy: reducing the effective mass of holes and significantly enhancing their mobility by modulating the metal vacancies ($V_M$s) in semiconductor metal oxides. It is shown that this strategy exhibits universality in all three transition metal oxides ($WO_3$, $TiO_2$ and $Bi_2O_3$), and ultimately achieves a photocurrent enhancement by a factor of 4.4 and a stability of more than 120 h in PEC water splitting applications. Calculations show that the formation of $V_W$ (tungsten vacancy) in $WO_3$ results in a positive shift of the valence band maximum ($VB_M$) and the creation of a "band-tailed state", as shown in Fig. 18a and c. Energy band calculations show that the effective mass $m^*$ of the hole decreases from 2.69 $m_0$ to 0.95 $m_0$ (65% reduction) after the introduction of the metal vacancy, which implies a significant increase in the hole mobility, as shown in Fig. 18b and d. Therefore, it can be concluded that the tungsten vacancy ($V_W$) reduces the effective mass of the hole, which enhances the hole mobility and makes the carrier separation more efficient. Xu et al.[173] constructed CoV-MOFs with ligand defects on the surface of $BiVO_4$ by photoelectrochemical

treatment, which enhances the interfacial bonding and inhibits the $V^{5+}$ dissolution. The optimized photoanode achieved a photocurrent density of 6.0 mA cm$^{-2}$ at 1.23 V and operated stably at 0.6 V for 500 hours. The ligand defects modulated the energy band structure to enhance the light absorption and charge transfer efficiency.

#### 5.2.4. Bandgap engineering

Strategies for bandgap engineering using semiconductor photocatalysts can influence the transport paths of electrons and holes, thereby improving carrier separation efficiency. In addition, altering the bandgap position can enhance their redox capabilities. Dong et al.[174] decorated the surface of coral-like $WO_3$/W films with hierarchical, flower-like arrays of stabilized heterogeneous (Co, Ni)-metal–organic framework (MOF) composites. The resulting (Co, Ni)-MOF/$WO_3$/W photoanode exhibited a high photocurrent density of 2.96 mA cm$^{-2}$ at 1.23 V vs. RHE in a 0.5 M neutral $Na_2SO_4$ electrolyte and achieved a solar-to-hydrogen (STH) efficiency of 2.17% under AM 1.5 G illumination. Light-assisted Kelvin probe force microscopy (KPFM) revealed the spatial distribution and segregation dynamics of photogenerated charges. The energy band alignment facilitated efficient charge separation: the conduction band (CB) of (Co, Ni)-MOF lies above that of $WO_3$, enabling spontaneous electron transfer from (Co, Ni)-MOF to $WO_3$. These electrons then traverse the $WO_3$/W Schottky junction to
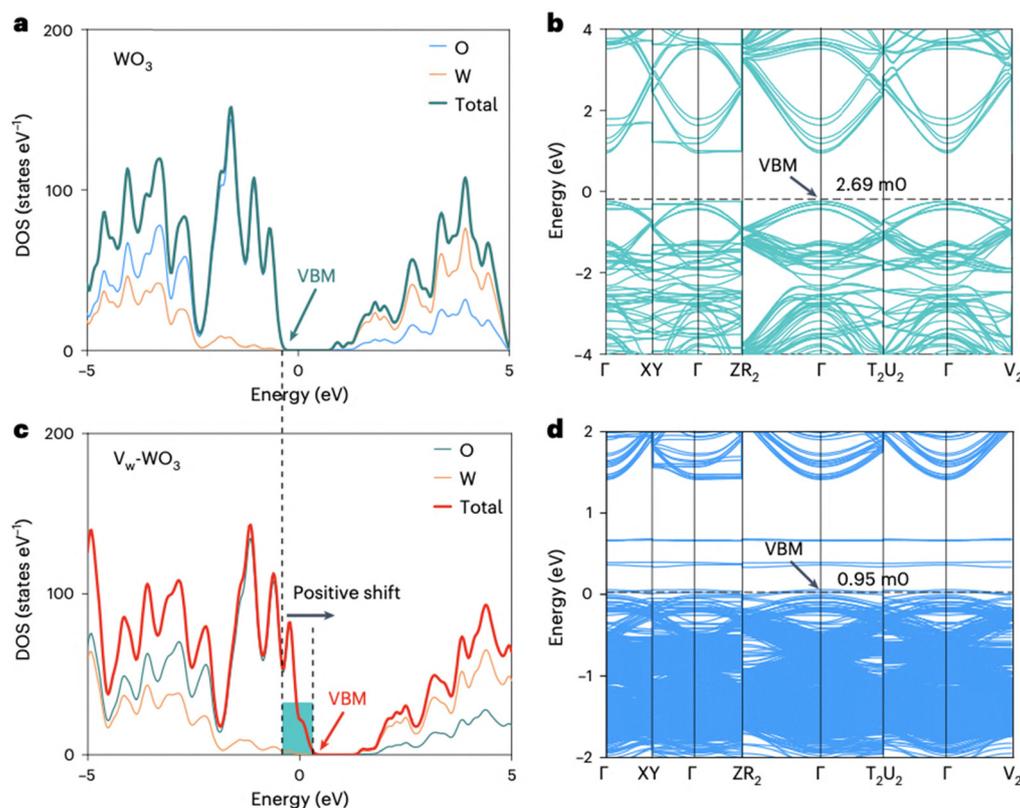


Fig. 18 Theoretical calculation of the energy band structures. (a) and (c), calculated density of states (DOS) of $WO_3$ (a) and Vw-$WO_3$ (c). (b) and (d), Energy band structures of $WO_3$ (b) and Vw-$WO_3$ (d).[172] Copyright 2025, Nature.
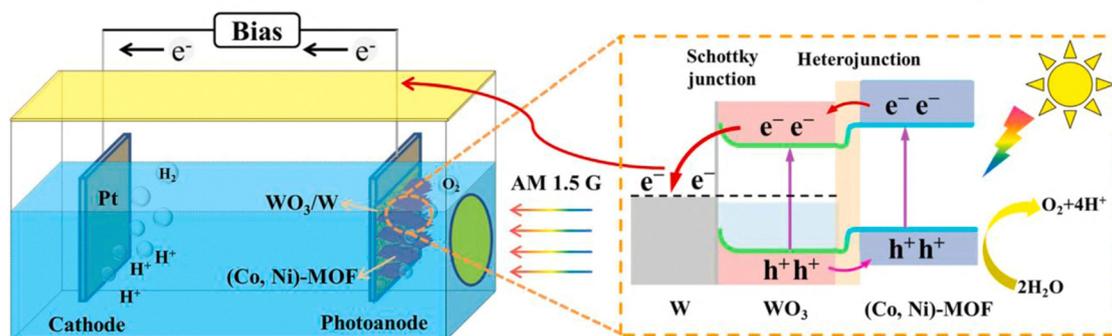
**Fig. 19** The schematic illustration of separation and transfer paths of photogenerated charges for the (Co, Ni)–MOF/WO₃/W photoanode during the PEC process.[174] Copyright 2024, Elsevier.

reach the cathode under bias, while the photogenerated holes accumulate in the valence band (VB) of (Co, Ni)-MOF and participate in the oxygen evolution reaction (OER), as illustrated in Fig. 19. This mechanism effectively suppresses charge recombination, enhancing solar-driven photoelectrochemical water splitting.

Li et al.[175] proposed a strategy to enhance the quasi-Fermi level of MIL-53 (Fe) by injecting high-energy electrons via EY, thereby boosting photocatalytic activity. The integration of characterization techniques and theoretical simulations revealed that dye sensitization is capable of efficiently injecting high-energy electrons into Fe-based metal–organic frameworks (Fe-MOFs) and raising their quasi-Fermi level upon light irradiation, as shown in Fig. 20. After EY has sufficiently elevated the quasi-Fermi level of Fe-MOFs under light irradiation,

depositing Pt nanoparticles on the Fe-MOF can reduce charge transfer resistance and improve charge separation, thereby lowering the overpotential for H₂ evolution.

## 5.3. Electrode reactions and generation of products

**5.3.1. Electrode reaction.** In the photoelectrocatalytic process, the electrode reaction is a crucial link between light absorption and product generation, which involves the migration and utilization of photogenerated charges and determines the products and efficiency of photoelectrocatalysis. Ideal electrode materials should have good electrical conductivity, sufficient electrochemical activity and good stability to support the charge transfer and reaction in the photoelectrocatalytic process. Metal-based, carbon-based, and composite electrodes are commonly used.[176–186] For example, Hu et al.[187] developed a
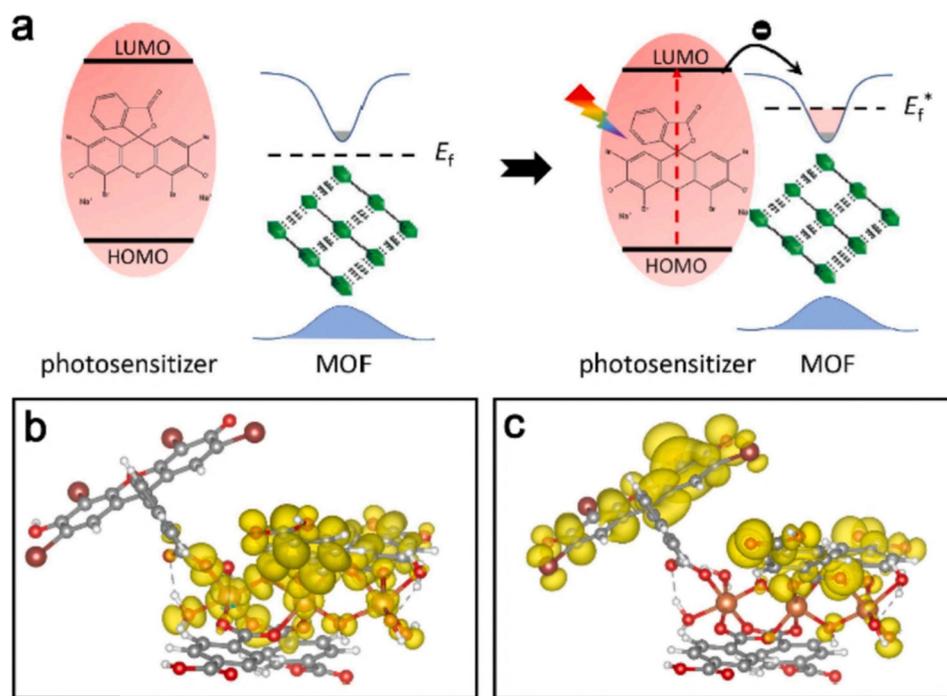


**Fig. 20** (a) Energy diagrams of MIL–53(Fe) before and after EY sensitization. (b and c) Side views of the charge densities at the EY-MIL–53(Fe) interface showing the electron unoccupied and occupied states. Color: white (H); grey (C); red (O); orange (Fe); brown (Br).[175] Copyright 2022, Elsevier.
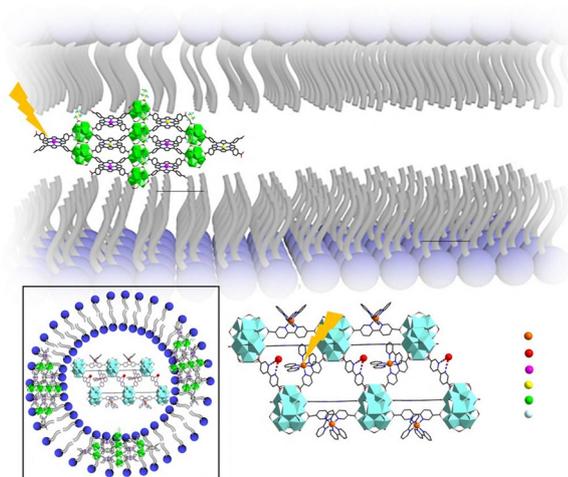
**Fig. 21** Structure of the LP–MOF for overall photocatalytic water splitting and the proposed 'Z-scheme' electron-transfer chain in the LP–MOF system. The bilayer in the illustration represents a section of the liposome. The HER-MOF for hydrogen evolution is incorporated between the hydrophobic chains, and the WOR-MOF for water oxidation is in the aqueous phase. The redox shuttles TCBQ/TCBQH and $Fe^{3+}/Fe^{2+}$ connect the HER and WOR sides, functioning in the lipid phase and the aqueous phase, respectively. Electron-transfer chains (shown by blue arrows) and photons (represented by yellow lightning shapes) form the 'Z-scheme'. Inset, schematic representation of the liposome with the two MOFs embedded within the hydrophobic bilayer (HER-MOF) and the hydrophilic interior (WOR-MOF).[187] Copyright 2021, Nature.

liposome-MOF assembly for integrated photocatalytic water splitting. This structure spatially separates HER-MOF and WOR-MOF nanosheets: the hydrophobic-modified HER-MOF (containing light-harvesting Zn–porphyrin and catalytic Pt-porphyrin) is embedded in the lipid bilayer; while WOR-MOF (containing $[Ru(bpy)_3]^{2+}$ photosensitizers and Ir-bipyridine catalysts) is positioned in the hydrophilic interior of the liposome, as shown in Fig. 21. This spatial separation effectively promotes photogenerated charge separation.

To gain a deeper understanding of the photoelectrocatalytic process, it is helpful to study the electrode reaction kinetics. For example, we can study the migration of photogenerated charges on the electrodes and the reaction process measured current–voltage curves and electrochemical impedance spectra,

which can help to optimize the electrode structure and improve the photoelectrocatalytic efficiency. For example, Yang et al.[149] coated the surface of $BiVO_4$ nanoarrays with a CoFe MOF (NA) nanolayer, resulting in the $BiVO_4$/CoFe MOF (NA) catalyst. EIS confirmed a significant reduction in interfacial resistance, as shown in Fig. 22a; the current–voltage curve showed a photo-current density of 3.92 mA cm$^{-2}$ at 1.23 V, a 6.03-fold increase compared to pure $BiVO_4$, due to significantly improved charge transfer and separation efficiency, as shown in Fig. 22b. At 400 nm, the BVO/CoFe MOF(NA) photoanode exhibits the highest IPCE, with an APCE as high as 96%, indicating that almost all absorbed photons at this wavelength effectively drive the water oxidation reaction, as shown in Fig. 22c.

Co-catalysts can improve the reactivity of photoelectro-catalysts and promote the splitting of water molecules and hydrogen generation on the surface of photoelectrocatalysts; certain co-catalysts with specific functions, such as noble metals and transition metal oxides, can improve the reactivity and establish an effective electron transport pathway by providing active centers or promoting the adsorption of intermediate species. For example, Wang et al.[188] investigated the effect of MOF-derived co-catalysts on the photocatalytic performance of $BiVO_4$ photoanodes. Porous $BiVO_4$-based thin films were prepared using electro-deposition and thermal annealing methods. The $BiVO_4$ electrodes were then immersed in a Co-MOF (ZIF-67) precursor solution, and the porous $BiVO_4$ surface was subjected to *in situ* modification at room temperature. The resulting $BiVO_4$-MOF photoanode was annealed at 450 °C for 2 hours in a $N_2$ atmosphere, converting the MOF into a carbon matrix containing cobalt-based active reaction centers, ultimately yielding the $BiVO_4$-MOF-$N_2$ catalyst. The MOF-derived co-catalyst significantly enhanced the photocurrent density of the $BiVO_4$-MOF-$N_2$ photocathode to 2.32 mA cm$^{-2}$ (1.23 V vs. RHE), approximately 2.64 times that of the pristine $BiVO_4$. Compared to the pure MOF co-catalyst, the MOF-derived co-catalyst exhibits higher charge transfer efficiency and lower charge transfer resistivity during the charge transfer process from $BiVO_4$ to the cobalt co-active center, due to the excellent conductivity of the carbon matrix.

**5.3.2. Generation of products.** The formation of products during photoelectrocatalysis depends on the mechanism and conditions of the electrode reaction. Ideally, the generation of
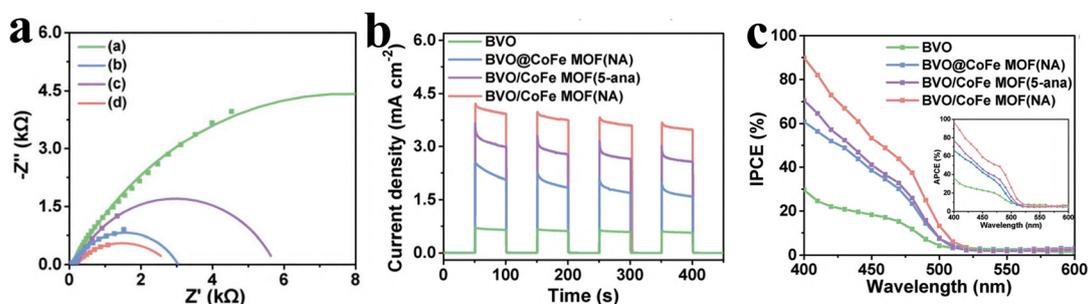


**Fig. 22** (a) EIS Nyquist plots under light irradiation. (b) Chopped light *i–t* curves of BVO, BVO@CoFe MOF(NA), BVO/CoFe MOF(5-ana), and BVO/CoFe MOF(NA). (c) IPCE spectra (inset shows the APCE spectra).[149] Copyright 2023, Wiley.

hydrogen and oxygen from the photoelectrocatalytic splitting of water should be in accordance with Faraday's law, but due to various factors in the actual reaction process, such as surface coverage, charge separation efficiency and so on, the actual proportion of products may deviate from the theoretical value, and it is recommended to optimize the reaction conditions and electrode structure in order to improve the product selectivity. Most single-phase photocatalysts designed for complete water splitting primarily respond to the ultraviolet region of sunlight, which constitutes a very small proportion of the spectrum. In light of this, He et al.[189] proposed a universal strategy that enables the internal ligands of MOFs to directly form ligand-cluster charge transfer (LCCT), which plays a dominant role, thereby achieving complete water splitting photocatalysis with broad response to visible light. Most single-phase photocatalysts designed for complete water splitting primarily respond to the small ultraviolet region of sunlight. In light of this, Professor He Jun and Associate Professor Liao Weiming from Guangdong University of Technology reported a universal strategy that enables the internal ligands of MOFs to directly form ligand-cluster charge transfer (LCCT) as the dominant mechanism, and this novel photocatalyst exhibits broad-spectrum response to visible light for complete water splitting photocatalysis.

The formation of photocatalytic products is influenced by various factors, including light conditions, temperature, pH, and different coupling reactions.[189–197] The formation of products in photoelectrocatalysis is significantly affected by light intensity and spectral distribution. Intense light increases the rate of photogenerated charge production, thus improving the efficiency of photoelectrocatalysis. However, excessive light can also cause problems such as photocorrosion and thermal effects, which can negatively affect the photoelectrocatalytic process. Therefore, it is crucial to select appropriate light conditions to optimize product generation. Therefore, selecting appropriate light conditions and designing suitable catalysts are critical for optimizing product formation. For example, metal sulfide photocatalysts are typically unsuitable as single-particle photocatalysts for water splitting due to photodegradation. Therefore, Iwashina et al.[198] utilized various metal sulfides as hydrogen-evolving photocatalysts and RGO-$TiO_2$ composites as oxygen-evolving photocatalysts for Z-diagram water splitting. When unloaded $CuGaS_2$ was combined with RGO-$TiO_2$ composites, $H_2$ and $O_2$ were not released in stoichiometric amounts, indicating that $H_2$ release was primarily due to photocorrosion. Pt particles loaded via adsorption served as effective hydrogen release sites, enabling $H_2$ and $O_2$ to be released in stoichiometric amounts while mitigating photocorrosion. Temperature has an important effect on the efficiency of PEC hydrolysis. The PEC efficiency of MOF materials can be effectively optimized by adjusting the temperature. The effect of temperature on the formation of photoelectrocatalytic products is mainly characterized by their influence on the adsorption properties of the reactants and the potential alteration of the chemical reaction pathways. In some cases, lower temperatures may lead to higher product selectivity, while higher

temperatures may promote chemical reactions. The pH of the solution also has a significant effect on the photoelectrochemical water splitting process. The normal operation of a PEC cell requires the electrolyte to be in a specific pH environment, so the equilibrium state of the PEC water splitting reaction will be largely regulated by the pH of the electrolyte solution. When the solution pH changes, the species adsorbed on the electrode surface and their charge states also change, which in turn affects the rate and efficiency of the PEC water splitting reaction. Variations in pH also can cause corrosion of the photoelectrode materials. So it is necessary to regulate the pH of the electrolyte and to design catalysts that are stable over a wide range of pH values.[199] The coupling reactions of hydrogen evolution reactions also affect the efficiency of water splitting. Hydrogen production can be promoted by replacing the slow OER with a thermodynamically more favorable reaction. For example, Zhou et al.[200] used the oxidation reaction of benzyl alcohol to benzaldehyde to replace the OER reaction. On a $Bi_2MoO_6$@$TiO_2$ NTA photocathode, the selectivity of benzyl alcohol conversion to benzaldehyde reaches 100%. The electrons generated in this controlled and selective one-step oxidation reaction are used as a source for synergistic hydrogen production. The hydrogen production rate is 5.5 times higher than when using the OER. The efficiency of this hydrogen production process reaches up to 85%. Photoelectrocatalytic electrode reactions and product generation processes are complex and involve multiple factors and processes. An in-depth understanding of the mechanism of photoelectrocatalytic electrode reactions and an in-depth study of the mechanism of photoelectrocatalytic reactions can help to improve the efficiency of photoelectrocatalysis.

## 5.4. Stability

In photocatalytic processes, catalyst stability is compromised by photodegradation, dissolution of active sites, or structural collapse. Therefore, catalyst stability is a key parameter for evaluating the performance of photocatalysts and is also critical to their reliability in practical applications. Research into stability enhancement strategies (such as ligand engineering, controlling the coordination environment, and adding co-catalysts) can lead to the development of highly stable photocatalysts.

**5.4.1. Ligand engineering.** The primary limitation preventing the use of MOFs in photocatalysis stems from their poor stability. In light of this, Dominik Eder et al.[201] prepared a mixed ligand ZIF-67 (AE) using ligand engineering. The study found that the single ligand ZIF (A) undergoes complete reconstruction (CR) during visible-light photocatalysis, with its framework gradually oxidizing and ultimately transforming into CoOOH, causing its intrinsic photoluminescence (PL) peak to shift significantly from 566 nm to 482 nm, and the bandgap to increase from 1.75 eV to 2.75 eV (Fig. 23a and b). In contrast, the mixed ligand AE-ZIF undergoes only surface reconstruction (SR), forming a cobalt oxide hydroxide protective layer on the surface in situ, effectively maintaining the stability of the main framework (Fig. 23d and e). This structural difference significantly impacts catalytic performance: A-ZIF exhibits a temporary increase in current
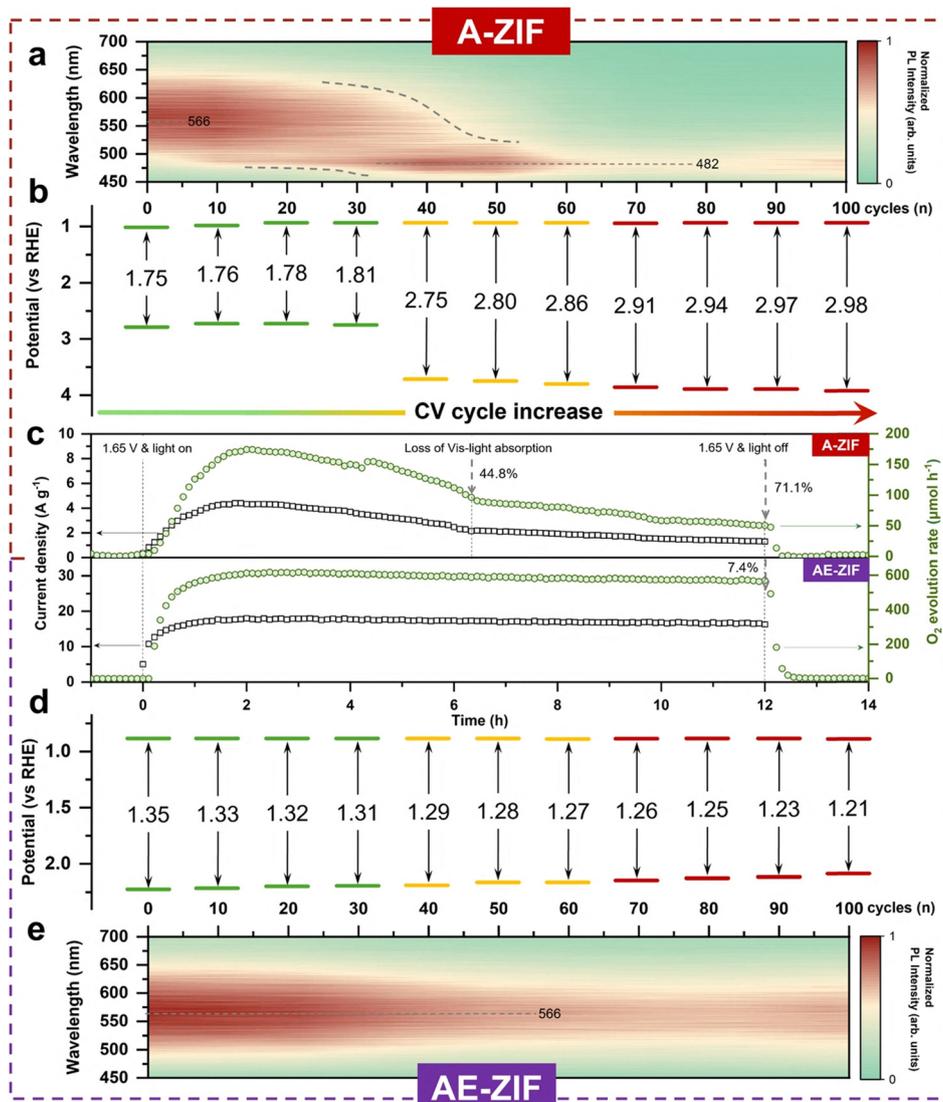
**Fig. 23** Photoelectrocatalytic OER activity, PL intensity and band gaps. (a) and (b) *In situ* electrochemical photoluminescence spectroscopy (a) and band potential diagram (b) of A-ZIF with 100 CV cycles at 0.85–1.55 V. (c) Amperometric plots and O₂ evolution rates of A-ZIF and AE-ZIF at certain potentials of 1.65 V and visible light. (d) and (e) Band potential diagram (d) and *in situ* electrochemical PL spectroscopy (e) of AE-ZIF with 100 CV cycles at 0.85–1.55 V. Copyright 2024, Elsevier.201 Copyright 2024, Nature.

density and $O_2$ release rate during the initial illumination phase (<2 hours), but its visible light absorption capability decreases due to the widened bandgap, resulting in performance dropping to near dark-state levels after 6 hours; in contrast, AE-ZIF maintains highly stable performance under illumination during a 12-hour chronoamperometry test, with initial efficiency rapidly improving due to the formation of the protective layer (Fig. 23c). The results indicate that the mixed ligand strategy significantly enhances the photocatalytic stability of ZIF by suppressing complete reconstruction. Subsequently, the efficiency decreased by only 7.4% after 12 hours. The bandgap of AE-ZIF undergoes only a small decrease from 1.35 to 1.21 eV, as only surface reconstruction occurs. All results indicate that mixed ligands can induce surface reconstruction to form an active protective layer, adapting to changes in the reaction environment and enhancing catalyst stability.

$BiVO_4$ is considered a promising photoanode material due to its suitable energy band structure. After years of development, although the oxygen precipitation activity of $BiVO_4$ photoanodes has been dramatically improved, the poor photostability of $BiVO_4$ photoanodes due to the dissolution of $V^{5+}$ ions during photoelectrocatalytic processes has become a bottleneck challenge that restricts its transition from the laboratory to practical applications. The main challenge of $BiVO_4$ photoanodes lies in their photocorrosion problems, especially the $V^{5+}$ dissolution leading to decreased stability. Xu *et al.*[173] designed $Co_3O_4$/CoV-MOF/BiVO photoanode catalysts, which, due to the presence of ligand defects and the formation of a large number of unpaired sites in CoV-MOF, are able to enhance $BiVO_4$ surface $V^{5+}$ bonding between $V^{5+}$ ions and CoV-MOF, thus effectively inhibiting the dissolution of $V^{5+}$ in
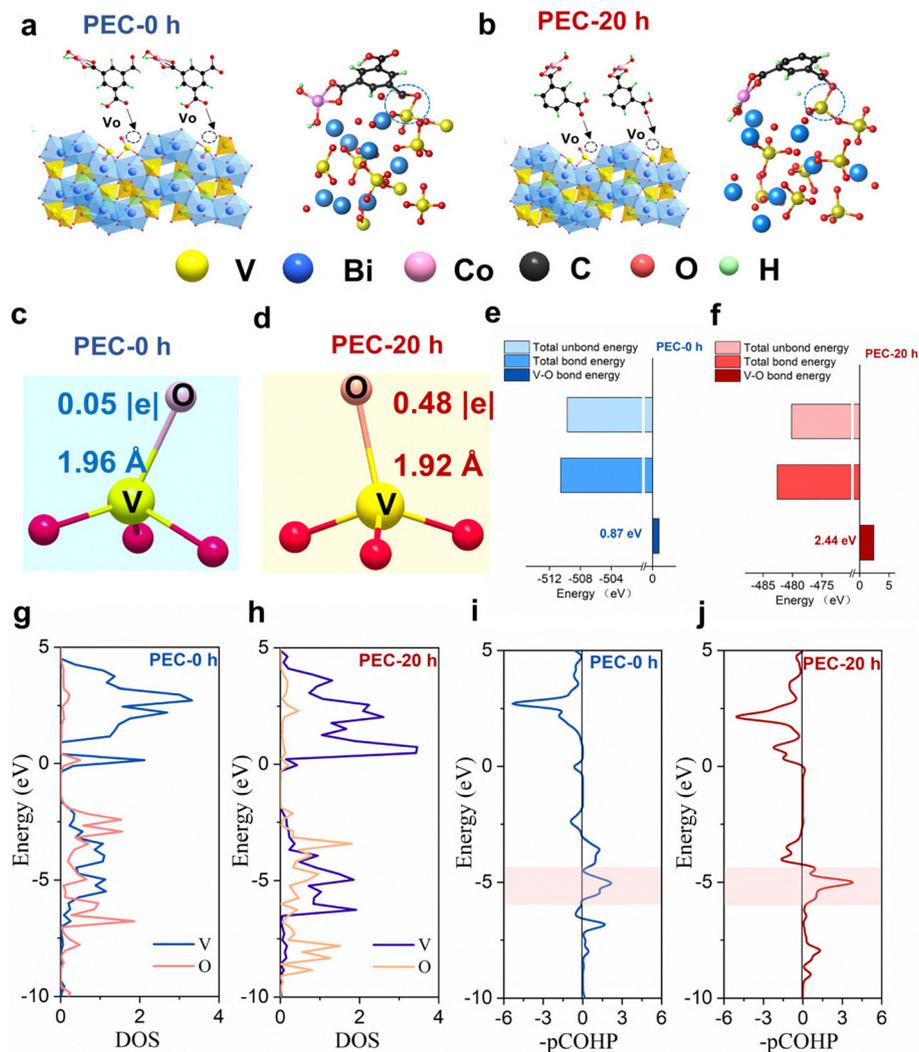
Fig. 24 Understanding the mechanisms of improved stability through PEC treatment. (a) and (b) Schematic diagrams of the interaction between different types of MOF molecules and BVO surface, where (a) is the CoV-MOF without ligand defects (PEC-0 h) and (b) is the CoV-MOF with ligand defects (PEC-20 h). Schematic diagrams of the electron transfer and bond length on interfacial V–O coordinated bonds for (c) PEC-0 h and (d) PEC-20 h. The interfacial V–O bond energy of (e) PEC-0 h and (f) PEC-20 h. Local DOS plots of (g) PEC-0 h and (h) PEC-20 h, and corresponding -pCOHP of V–O bonds for (i) PEC-0 h and (j) PEC-20 h.[108] Copyright 2025, ACS.

BiVO$_4$ during the hydrolysis process, and significantly improving photostability, stable operation for 500 h at 0.6 VRHE. The interfacial V–O coordination bonds of PEC-0 h without ligand defects and PEC-20 h with ligand defects are shown in Fig. 24a and b, respectively, where the carboxyl group in CoV-MOF interacts with the oxygen vacancies in the vanadium–oxygen tetrahedra of BVO to form a V–O coordination bond. As shown in Fig. 24c and d, the interfacial V–O bond of PEC-20 h has a shorter bond length of about 1.92 nm compared with that of PEC-0 h. Bader charge analysis of the O atoms also indicates that the electron transfer in PEC-20 h (0.48 e) is higher than that in PEC-0 h (0.05 e). As shown in Fig. 21e and f, PEC-20 h with ligand defects showed a larger V–O binding energy of 2.44 eV. In contrast, the V–O binding energy of PEC-0 h was only 0.87 eV, which is consistent with the V–O bond length. Fig. 24g–j show the localized density of states (DOS) and the corresponding pCOHP of the V–O bonds of PEC-0 and PEC-20 h. It is clear that the V–O bond of PEC-20 h exhibits a larger overlap of the density of states, which implies that the interaction between V and O atoms is stronger. The pCOHP effectively reflects the charge distribution and chemical bonding properties. The more positive the pCOHP value is below the Fermi energy level, the more bonding states there are and the stronger the bonds are. In Fig. 24i and j, PEC-20 h shows stronger bonding states. Thus, the PEC treatment leads to ligand defects in CoV-MOF, effectively inhibits the dissolution of V atoms from the BVO lattice and leads to ultra-stable hydrolysis properties.

**5.4.2. Introduction of a co-catalyst.** Photocatalytic corrosion refers to the gradual decomposition of a material under light exposure due to its own redox reactions. Essentially, the photogenerated charges (electrons and holes) are not effectively
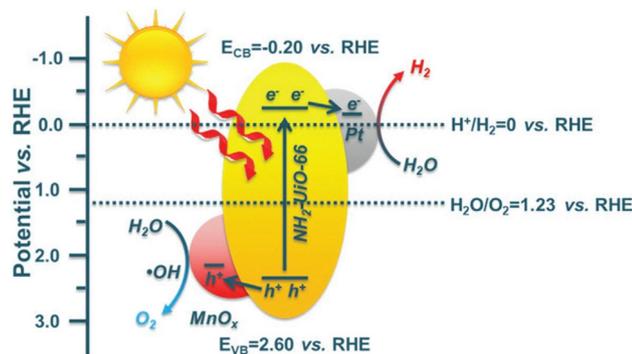
**Fig. 25** Schematic presentation of the reaction process of overall water splitting with the PUM sample under visible light irradiation.[202]

utilized in the water splitting reaction but instead participate in the chemical reactions of the catalyst's own components. The methods for enhancing charge separation mentioned in Section 4.2 can effectively mitigate photocorrosion. Additionally, co-catalysts can be introduced. Co-catalysts promote charge separation, reduce the recombination of photo-generated carriers within the catalyst, thereby mitigating oxidation corrosion caused by hole accumulation, and significantly enhancing the chemical stability of MOF catalysts in PEC water splitting. Zhang et al.[202] developed a Pt@NH$_2$-UiO-66@MnO$_x$ (PUM) heterojunction photocatalyst with spatially separated co-catalysts (Pt and MnO$_x$) for efficient water splitting. Compared to pure NH$_2$-UiO-66 (PU), PUM exhibited significantly enhanced photocatalytic activity. This catalyst combines high activity and excellent stability among reported UiO-66-based materials, with only a 0.6% activity decline after six cycles. In this system, the Pt co-catalyst captures electrons, while MnO$_2$ collects holes (Fig. 25). Photogenerated charge carriers (electrons and holes) migrate within and outside the MOF and accumulate on the corresponding co-catalysts to participate in redox reactions, effectively suppressing electron–hole recombination and prolonging their lifetime. All these results indicate that the presence of spatially separated co-catalysts

enables more efficient separation of photogenerated carriers and an increase in photoreactivity, while avoiding reverse reactions and suppressing photocorrosion.

## 6. Conclusion and prospects

Recent advancements in the utilization of MOFs and derivatives for the photoelectrocatalytic splitting of water are reviewed. Studies have demonstrated the robust catalytic activity of MOFs and their derivatives in this process. Various critical factors influencing photoelectrocatalytic hydrogen production are extensively analyzed, including light absorption and utilization, charge separation and transport, surface activity and catalyst stability. Despite the promising prospects of this technology, it is confronted with certain challenges and constraints.

1. Although MOFs are a class of crystalline porous materials with tunable pore sizes, they have been shown to be highly suitable for integrating different catalytic active species into the pore space to enhance catalytic activity. For example, MOFs can be used to accommodate metal nanoclusters. However, controlling the size of MOF pores is challenging.[203] Furthermore, photocatalytic water splitting is a liquid-phase dynamic process, and the accessibility of active sites is a critical parameter, with the diffusion of reactants being limited by the inherent small pore size. Therefore, it is essential to exploit the potential of pore engineering to improve the performance of MOFs in diverse liquid-phase applications.[204]

2. The bandgap of MOF is usually wide and only absorbs UV light with low utilization of visible light, limiting the solar energy conversion efficiency.

3. Certain MOFs are prone to decomposition in aqueous solutions or when exposed to light, particularly becoming significantly deactivated over prolonged reaction times, and specific organic ligands being easily degraded by additional oxidants. Consequently, there exists an urgent need for the development of high-efficiency and stable MOF photocatalysts.
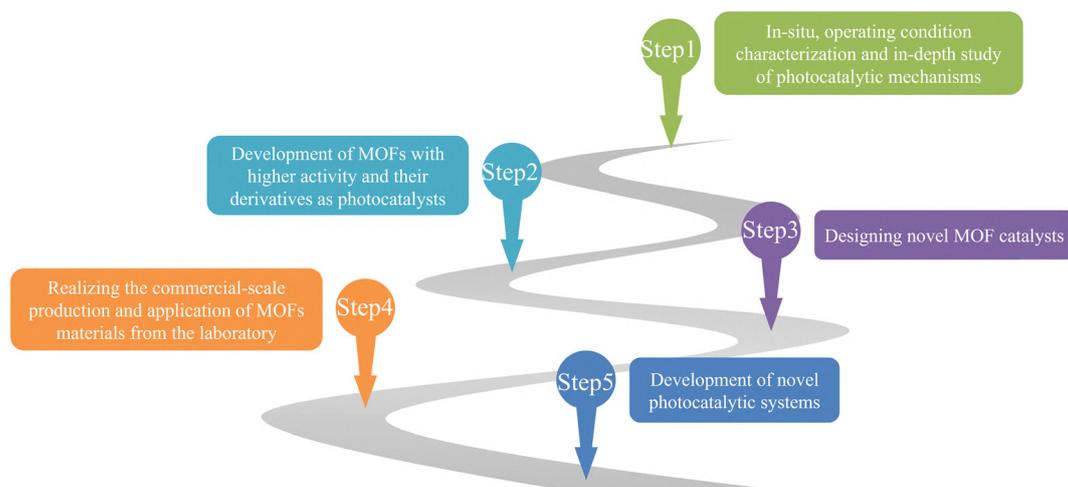


**Fig. 26** Future development directions for MOF photocatalysts.

4. The high interfacial resistance between the organic ligands and inorganic nodes of MOF makes the photogenerated electron–hole pairs easy to be compounded, resulting in short carrier lifetime.

5. Scaling up the synthesis of MOFs from laboratory scale to industrial production poses significant challenges, primarily due to their high production costs and poor reproducibility. Therefore, corresponding measures need to be taken to promote the commercialization and industrialization of MOFs.

Future direction of development:

The key to photocatalytic hydrogen production technology is to improve the efficiency of photocatalysis and hydrogen yield. To meet this challenge, significant efforts are still needed. MOF materials used for water splitting can be explored in the following aspects, as shown in Fig. 26.

1. *In situ* characterization: characterizing photocatalytic and photoelectrocatalytic mechanisms under *in situ* conditions is intricate. Employing time-resolved spectroscopy and *operando* techniques is essential to dynamically monitor the reaction interface process. This approach allows for a comprehensive and precise understanding of the role of MOF-based materials in the photoelectrocatalytic mechanism. Investigating photogenerated charge generation, transfer, and reaction processes, is conducive to elucidating the kinetic mechanism of photoelectrocatalytic hydrogen production reactions, offering a more scientifically grounded foundation for optimizing reaction conditions. These studies will serve as a theoretical roadmap for designing highly efficient catalysts.

2. Develop next-generation MOFs/MOF-derived photocatalysts with higher activity. Design strategies: (1) precise control: precisely control the coordination patterns of metal nodes (coordination number, geometric configuration) and organic ligands (conjugated nature, connectivity) to precisely coordinate and regulate the charge transfer pathways of MOFs. (2) Multilevel pore structure design. Pores of different sizes serve distinct functions, *e.g.*, micropores ($<2$ nm) provide active sites, mesopores (2–50 nm) facilitate mass transfer, and macropores ($>50$ nm) enhance light penetration.[205–207] This can enhance activity by adjusting the pore structure of MOFs. (3) Heterostructure construction and interface engineering: Improve carrier separation efficiency. (4) Interdisciplinary integration: drawing inspiration from artificial photosynthesis systems (*e.g.*, liposome-MOF) and energy materials (*e.g.*, perovskite solar cells) to advance the development of novel photoanodes.[208,209] (5) Development of co-catalysts: some high-performance co-catalysts can significantly enhance the efficiency of photocatalytic hydrogen production. For example, when metal oxides such as $MnO_x$ form heterojunction structures with MOF catalysts and their derivatives, electrons and holes accumulate on the co-catalyst and participate in redox reactions, prolonging the lifetime of photo-generated electrons and holes, thereby facilitating electron–hole separation and improving hydrogen production efficiency. Additionally, precious metals such as Pt and Pd are commonly used as co-catalysts to provide active sites that promote water splitting. In the future, the development of efficient and stable composite co-catalysts could further enhance the performance and stability of photocatalytic hydrogen production.

3. Design of novel MOFs; currently, commonly used MOF templates include zeolitic imidazolate frameworks (ZIFs), University of Oslo (UiO), and Material Institute of Lavoisier (MIL). It is necessary to explore novel MOFs with designed structures and active sites. By precisely arranging the active sites and synergistically combining them with multi-level structures, their light absorption capacity, charge separation, and migration performance can be improved.

4. The transition of MOF materials from laboratory-scale synthesis to commercial-scale production and application faces several challenges. (1) Presently, standardized protocols for the synthesis and characterization of porous materials are insufficient. The absence of standardized methods makes it challenging to compare different research results and ensure experimental reproducibility. For example, establishing databases, promoting data sharing, and enhancing research transparency can significantly improve the reproducibility of porous material research. At the same time, strict control of synthesis parameters (such as time, temperature, pressure, concentration, flow rate, specific surface area, *etc.*) is key to ensuring technical reproducibility and reducing costs.[133] (2) Process greening: promote atmospheric pressure aqueous phase synthesis and continuous flow technology, and phase out high-energy-consuming high-pressure reactions.[210,211] Raw material recycling: Establish a waste ligand/waste MOF recycling network to promote the high-value utilization of industrial waste.[212]

5. Development of novel photocatalytic systems: Future research must prioritize the design of innovative system architectures, optimize the integration of photocatalytic devices and systems, reduce costs, and enhance practicality. Additionally, reaction conditions must be optimized, and stringent energy efficiency metrics must be established.

Overall, metal–organic frameworks (MOFs) and derivatives offer unique advantages not present in conventional materials, making them a promising platform for advancing photocatalysis and photoelectrocatalysis in energy and environmental contexts. The continuous technological progress enabling a more comprehensive exploration of these materials underscores their potential for future applications in energy and beyond.

## Conflicts of interest

There are no conflicts to declare.

## Data availability

No primary research results, software or code have been included and no new data were generated or analysed as part of this review.

## Acknowledgements

# References

1 X. W. Lv, W. W. Tian and Z. Y. Yuan, *Electrochem. Energy Rev.*, 2023, **6**, 23.

2 J. G. Hou, Y. Z. Wu, B. Zhang, S. Y. Cao, Z. W. Li and L. C. Sun, *Adv. Funct. Mater.*, 2019, **29**, 1808367.

3 Y. J. Li, L. Zhou and S. J. Guo, *EnergyChem.*, 2021, **3**, 100053.

4 G. Chen, C. Wei, Y. P. Zhu and H. T. Huang, *EcoMat.*, 2023, **5**, e12294.

5 X. Xiao, L. J. Yang, W. P. Sun, Y. Chen, H. Yu, K. K. Li, B. H. Jia, L. Zhang and T. Y. Ma, *Small*, 2022, **18**, 2105830.

6 Z. X. Li, M. L. Hu, P. Wang, J. H. Liu, J. S. Yao and C. Y. Li, *Coord. Chem. Rev.*, 2021, **439**, 213953.

7 C. L. Luo, X. J. Liu, K. Yang, J. Xu, Z. J. Zhu, Z. H. Tang, S. L. Shen, J. C. Fan, D. Luo, N. A. H. Alshammari, Z. M. El-Bahy, X. T. Xu, Y. H. Xue and L. K. Pan, *Coord. Chem. Rev.*, 2024, **516**, 215936.

8 H. S. Su, X. X. Chang and B. J. Xu, *Chin. J. Catal.*, 2022, **43**, 2757–2771.

9 S. T. Nishioka1, F. E. Osterloh, X. C. Wang, T. E. Mallouk and K. Maeda, *Nat. Rev. Methods Primers*, 2023, **3**, 42.

10 S. Lin, H. W. Huang, T. Y. Ma and Y. H. Zhang, *Adv. Sci.*, 2021, **8**, 20024258.

11 C. F. Fu, X. J. Wu and J. L. Yang, *Adv. Mater.*, 2018, **30**, 1802106.

12 K. Sun, Y. Y. Qian and H. L. Jiang, *Angew. Chem., Int. Ed.*, 2023, **62**, e202217565.

13 C. B. Bie, L. X. Wang and J. G. Yu, *Chem*, 2022, **8**, 1567–1574.

14 V. H. Dang, T. A. Nguyen, M. V. Le, D. Q. Nguyen, Y. H. Wang and J. C. S. Wu, *Chem. Eng. J.*, 2024, **484**, 149213.

15 L. H. Lin, T. Hisatomi, S. S. Chen, T. Takata and K. Domen, *Trends Chem.*, 2020, **2**, 813–824.

16 T. T. Yao, X. R. An, H. X. Han, J. Q. J. Chen and C. Li, *Adv. Energy Mater.*, 2018, **8**, 1800210.

17 J. Z. Jia, Y. T. Wang, Y. Y. Cha, Z. W. Wang, J. F. Huang, D. N. Wang, H. Li, K. L. Guo, J. Li, J. E. Huang, Y. Tang and C. L. Xu, *Adv. Funct. Mater.*, 2025, 2500568.

18 K. Poonia, P. Singh, A. Singh, A. Singh, S. Thakur, Q. V. Le, T. Ahamad, P. Raizada, C. Y. Wang, L. H. Nguyen and V. H. Nguyen, *Environ. Chem. Lett.*, 2023, **21**, 265–283.

19 Y. Huang, L. Zou, Y. B. Huang and R. Cao, *Chin. J. Catal.*, 2025, **70**, 207–229.

20 L. Y. Yang, F. Li and Q. J. Xiang, *Mater. Horiz.*, 2024, **11**, 1638–1657.

21 D. Liu, X. Y. Wan, T. T. Kong, W. W. Hanc and Y. J. Xiong, *J. Mater. Chem. A*, 2022, **10**, 5878–5888.

22 Z. R. Liu, X. Yu and L. L. Li, *Chin. J. Catal.*, 2020, **41**, 534–549.

23 L. V. Bora and N. V. Bora, *Fuel*, 2025, **381**, 133642.

24 T. T. Wu, G. Q. Deng and C. Zhen, *J. Mater. Sci. Technol.*, 2021, **73**, 9–22.

25 C. Y. Toe, S. J. Zhou, M. Gunawan, X. X. Lu, Y. H. Ng and R. Amal, *J. Mater. Chem. A*, 2021, **9**, 20277–20319.

26 K. R. G. Lim, A. D. Handoko, S. K. Nemani, B. Wyatt, H. Y. Jiang, J. W. Tang, B. Anasori and Z. W. She, *ACS Nano*, 2020, **14**, 10834–10864.

27 T. Tong, M. M. Zhang, W. F. Chen, X. Q. Huo, F. H. Xu, H. C. Yan, C. Lai, W. J. Wang, S. Y. Hu, L. Qin and D. L. Huang, *Coord. Chem. Rev.*, 2024, **500**, 215498.

28 F. Qiao, *Nano Res. Energy*, 2025, **4**, e9120132.

29 W. W. Li, J. L. Shi, K. H. L. Zhang and J. L. MacManus-Driscoll, *Mater. Horiz.*, 2020, **7**, 2832–2859.

30 Y. Zhang, Y. Y. Zhou, D. L. Sun, Y. X. Nie, D. Y. Wu, L. Ban, B. Tang, S. Yang, H. Li, T. Y. Ma and H. Zhang, *Coord. Chem. Rev.*, 2025, **527**, 216395.

31 S. Ali, S. H. Bakhtiar, A. Ismail, P. M. Ismail, S. Hayat, A. Zada, X. Q. Wu, A. N. Alodhayb, M. Zahid, F. Raziq, J. B. Yi and L. Qiao, *Coord. Chem. Rev.*, 2025, **523**, 216237.

32 X. D. Wang, J. L. Xie and C. M. Li, *J. Mater. Chem. A*, 2015, **3**, 1235–1242.

33 C. H. Jiang, Y. H. Zheng, W. G. Yang and F. R. Wan, *J. Univ. Sci. Technol.*, 2007, **29**(2), 139–141.

34 H. An, B. Lin, C. Xue, X. Q. Yan, Y. Z. Dai, J. J. Wei and G. D. Yang, *Chin. J. Catal.*, 2018, **39**, 654–663.

35 G. J. Liu, S. Ye, P. L. Yan, F. Q. Xiong, P. Fu, Z. L. Wang, Z. Chen, J. Y. Shi and C. Li, *Energy Environ. Sci.*, 2016, **9**, 1327–1334.

36 B. P. Mishraa and K. Parida, *J. Mater. Chem. A*, 2021, **9**, 10039–10080.

37 L. Mao, X. Y. Cai, H. Gao, X. G. Diao and J. Y. Zhang, *Nano Energy*, 2017, **39**, 172–182.

38 S. Mondal, G. Mark, L. Abisdris, J. Y. Li, T. Shmila, J. Tzadikov, M. Volokh, L. D. Xing and M. Shalom, *Mater. Horiz.*, 2023, **10**, 1363–1372.

39 W. W. Yu, T. Zhang and Z. K. Zhao, *Appl. Catal., B*, 2020, **278**, 119342.

40 M. J. Wang, M. Langer, R. Altieri, M. Crisci, S. Osella and T. Gatti, *ACS Nano*, 2024, **18**(13), 9245–9284.

41 M. Ali, A. S. Anjum, A. Bibi, S. Wageh, K. C. Sun and S. H. Jeong, *Carbon*, 2022, **196**, 649–662.

42 H. Xiao, W. X. Wang, M. Zhao, Z. M. Fu, M. Bai, L. Zhang, J. M. Zhang, E. G. Luo, J. Zhang, H. S. Wu and J. F. Jia, *Chem. Eng. J.*, 2024, **490**, 151415.

43 Y. d Pan, R. Abazari, B. Tahir, S. Sanati, Y. C. Zheng, M. Tahir and J. K. Gao, *Coord. Chem. Rev.*, 2024, **499**, 215538.

44 Y. J. He, W. Liu and J. Q. Liu, *J. Colloid Interface Sci.*, 2024, **661**, 409–435.

45 Z. Wang, X. D. Jin, L. P. Yan, Y. Z. Yang and X. G. Liu, *Microchim. Acta*, 2023, **190**, 28.

46 D. d Hu, R. T. Guo, J. S. Yan, S. H. Guo and W. G. Pan, *Nanoscale*, 2024, **16**, 2185–2219.

47 X. L. Li, S. S. Rajasree, J. R. Yu and P. Deria, *Dalton Trans.*, 2020, **49**, 12892–12917.

48 A. Thiam, J. A. Lopez-Ruiz, D. Barpaga and S. Garcia-Segura, *Molecules*, 2021, **26**, 5713.

49 H. L. Zhu, D. X. Liu, D. T. Zou and J. Y. Zhang, *J. Mater. Chem. A*, 2018, **6**, 6130–6154.

50 A. García-Sánchez, M. Gomez-Mendoza, M. Barawi, I. J. Villar-Garcia, M. Liras, F. Gándara and V. A. de la Peña O'Shea, *J. Am. Chem. Soc.*, 2020, **142**(1), 318–326.

51 Q. K. Shi, M. Cheng, Y. Liu, J. Wang, G. X. Zhang, L. Li, L. Du, G. F. Wang and H. D. Liu, *Coord. Chem. Rev.*, 2024, **499**, 215500.

52 J. Patel, G. Bury and Y. L. Pushkar, *Small*, 2024, **20**, 2310106.

53 J. Wang, C. Xue, W. Q. Yao, J. Liu, X. X. Gao, R. L. Zong, Z. Yang, W. J. Jin and D. P. Tao, *Appl. Catal., B*, 2019, **250**, 369–381.

54 R. Ifraemov, R. Shimoni, W. H. He, G. M. Penga and I. Hod, *J. Mater. Chem. A*, 2019, 7, 3046–3053.

55 S. Gulati, S. Vijaya, Mansi, S. Kumar, B. Harikumar, M. Trivedi and R. S. Varma, *Coord. Chem. Rev.*, 2023, **474**, 214853.

56 H. Furukawa, K. E. Cordova, M. O'Keeffe and O. M. Yaghi, *Science*, 2013, **341**, 1230444.

57 H. Wang, X. Yuan, Y. Wu, X. Chen, L. Leng and G. Zeng, *J. Hazard. Mater.*, 2015, **300**, 393–403.

58 M. Ali, E. Pervaiz, T. Noor, O. Rabi, R. Zahra and M. H. Yang, *Int. J. Energy Res.*, 2020, 1–37.

59 L. V. Bora and N. V. Bora, *Fuel*, 2025, **381**, 133642.

60 F. H. Mu, B. L. Dai, W. Zhao, L. L. Zhang, J. M. Xu and X. J. Guo, *Chin. Chem. Lett.*, 2020, **31**, 1773–1781.

61 L. Y. Yang, F. Li and Q. J. Xiang, *Mater. Horiz.*, 2024, **11**, 1638.

62 T. T. Yao, X. R. An, H. X. Han, J. Q. J. Chen and C. Li, *Adv. Energy Mater.*, 2018, **8**, 1800210.

63 J. Liu, W. Fu, Y. Liao, J. Fan and Q. Xiang, *J. Mater. Sci. Technol.*, 2021, **91**, 224–240.

64 Y. Li, D. Zhang, J. Fan and Q. Xiang, *Chin. J. Catal.*, 2021, **42**, 627–636.

65 M. A. Marwat, M. Humayun, M. W. Afridi, H. Zhang, M. R. Abdul Karim and M. Ashtar, *ACS Appl. Energy Mater.*, 2021, **4**, 12007–12031.

66 F. Li, X. Yue, L. Cheng, J. Fan and Q. Xiang, *Chem. Eng. J.*, 2023, **452**, 139463.

67 J. Chen, R. Abazari, K. A. Adegoke, N. W. Maxakato, O. S. Bello, M. Tahir, S. Tasleem, S. Sanati, A. M. Kirillov and Y. T. Zhou, *Coord. Chem. Rev.*, 2022, **469**, 214664.

68 S. Cho, J. W. Jang, K. H. Lee and J. S. Lee, *APL Mater.*, 2014, **2**, 010703.

69 J. J. Cen, Q. Y. Wu, M. Z. Liu and A. Orlov, *Green Energy Environ.*, 2017, **2**(2), 100–111.

70 R. T. Gao, X. T. Guo, S. J. Liu, X. Y. Zhang, X. H. Liu, Y. G. Su and L. Wang, *Appl. Catal., B*, 2022, **304**, 120883.

71 Z. Lin, Y. Q. Wang, Z. M. Peng, Y. C. Huang, F. Q. Meng, J. L. Chen, C. L. Dong, Q. H. Zhang, R. Z. Wang, D. M. Zhao, J. Chen, L. Gu and S. H. Shen, *Adv. Energy Mater.*, 2022, 2200716.

72 L. T. Shi, C. C. Wu, Y. Wang, Y. H. Dou, D. Yuan, H. Li, H. W. Huang, Y. Zhang, I. D. Gates, X. D. Sun and T. Y. Ma, *Adv. Funct. Mater.*, 2022, 2202571.

73 W. W. Zhang, L. J. Chen, S. Dai, C. X. Zhao, C. Ma, L. Wei, M. H. Zhu, S. Y. Chong, H. F. Yang, L. J. Liu, Y. Bai, M. J. Yu, Y. J. Xu, X. W. Zhu, Q. Zhu, S. H. An, R. S. Sprick, M. A. Little, X. F. Wu, S. Jiang, Y. Z. Wu, Y. B. Zhang, H. Tian, W. H. Zhu and A. I. Cooper, *Nature*, 2022, **604**, 72.

74 T. Bak, J. Nowotny, M. Rekas and C. C. Sorrell, *Int. J. Hydrogen Energy*, 2002, **27**, 991–1022.

75 Y. W. Dong, H. J. Liu, X. Wang, F. L. Wang, X. Y. Zhang, Q. X. Lv, C. Y. Liu, Y. M. Chai and B. Dong, *Appl. Catal., B*, 2023, **328**, 122464.

76 M. Li, Q. Wang, Y. He, Y. Wang, K. Wang, P. Tsiakaras and S. Song, *Coord. Chem. Rev.*, 2023, **495**, 215373.

77 N. E. Gorji, U. Reggiani and L. Sandrolini, *Sol. Energy*, 2012, **86**(3), 920–925.

78 H. Dotan, K. Sivula, M. Grätzel, A. Rothschild and S. C. Warren, *Energy Environ. Sci.*, 2011, **4**(3), 958–964.

79 B. K. Kim, M. J. Kim and J. J. Kim, *Appl. Catal., B*, 2022, **308**, 121226.

80 G. Heidari, M. Rabani and B. Ramezanzadeh, *Int. J. Hydrogen Energy*, 2017, **42**, 9545–9552.

81 F. A. Chaves, P. C. Feijoo and D. Jimenez, *Nanoscale Adv.*, 2020, **2**, 3252–3262.

82 S. Hamrouni, M. S. AlKhalifah, M. S. El-Bana, S. K. Zobaidi and S. Belgacem, *Appl. Phys. A: Mater. Sci. Process.*, 2018, **124**, 555.

83 G. Kear and F. C. Walsh, The characteristics of a true Tafel slope, *Corrosion Mater.*, 2005, **30**(6), 51–55.

84 A. J. Bard, L. R. Faulkner, J. Leddy and C. G. Zoski, *Electrochemical Methods: Fundamentals and Applications*, Wiley, New York, NY, 1980, vol. 2.

85 Y. N. Guo, T. Park, J. W. Yi, J. Henzie, J. Kim, Z. L. Wang, B. Jiang, Y. Bando, Y. Sugahara, J. Tang and Y. Yamauchi, *Adv. Mater.*, 2019, **31**(17), 1807134.

86 Y. Zhang, H. Lv, Z. Zhang, L. Wang, X. Wu and H. Xu, *Adv. Mater.*, 2021, **33**, 2008264.

87 M. Tahir, L. Pan, F. Idrees, X. W. Zhang, L. Wang, J. J. Zou and Z. L. Wang, *Nano Energy*, 2017, **37**, 136–157.

88 J. H. Li, Y. S. Wang, Y. C. Chen and C. W. Kung, *Appl. Sci.*, 2019, **9**(12), 2427.

89 W. W. Zhan, Q. Kuang, J. Z. Zhou, X. J. Kong, Z. X. Xie and L. S. Zheng, *J. Am. Chem. Soc.*, 2013, **135**(5), 1926–1933.

90 T. Y. Ma and S. Dai, *J. Am. Chem. Soc.*, 2014, **136**(39), 13925–13931.

91 M. Ding, X. Cai and H. L. Jiang, *Chem. Sci.*, 2019, **10**(44), 10209–10230.

92 M. Fujita, Y. J. Kwon, S. Washizu and K. Ogura, *J. Am. Chem. Soc.*, 1994, **116**(3), 1151–1152.

93 M. Alvaro, E. Carbonell, B. Ferrer, F. X. Llabrés i Xamena and H. Garcia, *Chem. – Eur. J.*, 2007, **13**, 5106–5112.

94 Z. T. Yu, Z. L. Liao, Y. S. Jiang, G. H. Li, G. D. Li and J. S. Chen, *Chem. Commun.*, 2004, 1814–1815.

95 P. Mahata, G. Madras and S. Natarajan, *J. Phys. Chem. B*, 2006, **110**, 13759–13768.

96 S. J. Liu, C. Zhang, Y. D. Sun, Q. Chen, L. F. He, K. Zhang, J. Zhang, B. Liu and L. F. Chen, *Coord. Chem. Rev.*, 2020, **413**, 213266.

97  B. Y. Chen, T. D. Hu, S. Y. Shan, Y. F. Zhi, C. R. Zhang and Q. Wu, *Acta Mater. Compositae Sin.*, 2022, **39**, 2073–2088.

98  Q. Q. Ge, M. Xu, X. Liang and F. W. Wang, *Chem. Ind. Eng. Prog.*, 2023, **42**, 4692–4705.

99  C. Pan, J. Y. Chao, F. S. Niu, S. H. Xie, H. Y. Gu, T. H. Su, K. Hu, D. W. Zhang, K. Liu, G. F. Liu, T. F. Xie, Z. T. Li and L. M. Zhang, *Adv. Mater. Interfaces*, 2022, **9**, 2101678.

100 J. Kosco, M. Bidwell, H. Cha, T. Martin, C. T. Howells, M. Sachs, D. H. Anjum, S. G. Lopez, Y. Zou, A. Wadsworth, W. M. Zhang, L. S. Zhang, J. Tellam, R. Sougrat, F. Laquai, D. M. DeLongchamp, J. R. Durrant and I. McCulloch, *Nat. Mater.*, 2020, **19**, 559–565.

101 X. F. Wu, D. S. Chen, W. Ma and K. K. Huang, *Chin. J. Appl. Chem.*, 2022, **39**(4), 694–696.

102 W. Liu, D. Y. Liu, Z. Y. Zhang and Z. K. Sun, *Particuology*, 2024, **91**, 19–28.

103 M. ChoeJin, Y. Koo, I. Park, H. Ohtsu, J. H. Shim, H. C. Choi and S. S. Park, *J. Am. Chem. Soc.*, 2022, **144**(37), 16726–16731.

104 L. T. Yu, J. Liu, X. J. Xu, L. G. Zhang, R. Z. Hu, J. W. Liu, L. Z. Ouyang, L. C. Yang and M. Zhu, *ACS Nano*, 2017, **11**(5), 5120–5129.

105 F. J. Claire, M. A. Solomos, J. Kim, G. Q. Wang, M. A. Siegler, M. F. Crommie and T. J. Kempa, *Nat. Commun.*, 2020, **11**, 5524.

106 S. J. Xie, Z. Y. Zhou, X. Zhang and J. Fransaer, *Chem. Soc. Rev.*, 2023, **52**, 4292–4312.

107 Q. Liu, Y. R. Miao, L. F. Villalobos, S. X. Li, H. Y. Chi, C. L. Chen, M. Tohidi Vahdat, S. Q. Song, D. J. Babu, J. Hao, Y. Han, M. Tsapatsis and K. V. Agrawal, *Nat. Mater.*, 2023, **22**, 1387–1393.

108 D. Balestri, Y. Roux, M. Mattarozzi, C. Mucchino, L. Heux, D. Brazzolotto, V. Artero, C. Duboc, P. Pelagatti, L. Marchi and M. Gennari, *Inorg. Chem.*, 2017, **56**(24), 14801–14808.

109 X. F. Li, M. Y. Lu, H. Y. Yu, T. H. Zhang, J. Liu, J. H. Tian and R. Z. Yang, *ChemElectroChem*, 2019, **6**(17), 4507–4510.

110 B. Gikonyo, F. B. Liu, S. Hawila, A. Demessence, H. G. Baldovi, S. Navalón, C. Marichy and A. Fateeva, *Molecules*, 2023, **28**(15), 5876.

111 W. M. A. El Rouby, M. Antuch, S. M. You and P. Millet, *Electrochim. Acta*, 2020, **339**, 135882.

112 P. Sindhu and N. Ballav, *Inorg. Chem.*, 2023, **62**(28), 10887–10891.

113 C. Young, J. Wang, J. Kim, Y. Sugahara, J. Henzie and Y. Yamauchi, *Chem. Mater.*, 2018, **30**(10), 3379–3386.

114 Y. W. Dong, X. J. Zhai, Y. Wu, Y. N. Zhou, Y. C. Li, J. Nan, S. T. Wang, Y. M. Chai and B. Dong, *J. Colloid Interface Sci.*, 2024, **658**, 258–266.

115 D. Cardenas-Morcoso, R. Ifraemov, M. García-Tecedor, I. Liberman, S. Gimenez and I. Hod, *J. Mater. Chem. A*, 2019, **7**, 11143–11149.

116 R. Tang, S. J. Zhou, L. Y. Zhang and L. W. Yin, *Adv. Funct. Mater.*, 2018, **28**, 1706154.

117 S. Q. Zhou, P. F. Yue, J. W. Huang, L. Wang, H. D. She and Q. Z. Wang, *Chem. Eng. J.*, 2019, **371**, 885–892.

118 D. B. Bailmare, B. V. Malozyomov and A. D. Deshmukh, *Commun. Chem.*, 2024, **7**, 178.

119 Y. J. Tang, H. Zheng, Y. Wang, W. Zhang and K. Zhou, *Adv. Funct. Mater.*, 2021, **31**, 2102648.

120 J. J. Feng, W. W. Li, T. X. Chen, Z. P. Zeng, M. Tian, W. X. Ji, Y. Guo, S. X. Min and X. Y. Liu, *Adv. Sci.*, 2025, **12**, 2411673.

121 M. Q. Xu, R. Zhang, J. He, Z. Y. Chen, J. C. Jiang, Z. X. Li, Y. J. Liu, D. Chen and Y. H. Ma, *Sep. Purif. Technol.*, 2025, **354**(5), 129093.

122 M. S. Xu, P. F. Zhu, Q. H. Cai, M. C. Bu, C. H. Zhang, H. Wu, Y. Z. He, M. Fu, S. Q. Li and X. Y. Liu, *Chin. Chem. Lett.*, 2024, **35**(10), 109524.

123 K. G. Tian, Z. Xu, H. Yang, G. L. Chen, P. F. An, J. Zhang, S. Z. Liu and J. Q. Yan, *Adv. Energy Mater.*, 2025, **15**, 2404477.

124 X. Y. He, Y. J. Ding, Z. N. Huang, M. Liu, M. F. Chi, Z. L. Wu, C. U. Segre, C. S. Song, X. Wang and X. W. Guo, *Angew. Chem.*, 2023, **62**, e202217439.

125 E. W. Liu, Z. L. Yang, L. J. Han, Y. P. Huang and K. K. Liao, *Acta Opt. Sin.*, 2021, **41**(07), 144–151.

126 Y. Z. Zhang, T. Cheng, Y. Wang, W. Y. Lai, H. Pang and W. Huang, *Adv. Mater.*, 2016, **28**, 5242–5248.

127 W. B. Wu, Z. X. Yang and T. L. Guo, *Chin. J. Vac. Sci. Technol.*, 2023, **43**(7), 563–568.

128 Y. C. Li, J. Su, Y. Zhao, L. Feng, L. Gao, X. Y. Xu, Y. Yin, Y. Yin, Y. F. Liu, P. W. Xiao, L. Yuan, J. S. Qin, Y. Y. Wang, S. Yuan, H. Zheng and J. L. Zuo, *J. Am. Chem. Soc.*, 2023, **145**(18), 10227–10235.

129 C. Wang, C. Liu, X. He and Z. M. Sun, *Chem. Commun.*, 2017, **53**, 11670–11673.

130 P. Liu, C. H. Zhou, Z. F. Ren, Q. Lin, Y. Zhou, J. Gu and Y. H. Shan, *Chem. Mater.*, 2021, **49**(12), 103–107.

131 S. Kouser, A. Hezam and S. A. Khanum, *J. Mol. Struct.*, 2025, **1321**, 140061.

132 W. M. Hu, Q. Ma, Y. Q. He, H. B. Liu, J. Q. Liu and X. H. Xia, *Chin. J. Inorg. Chem.*, 2020, **36**(3), 485–493.

133 M. Nazari, F. Zadehahmadi, M. M. Sadiq, A. L. Sutton, H. Mahdavi and M. R. Hill, *Commun. Mater.*, 2024, **5**, 170.

134 T. Paul, A. Juma, R. Alqerem, G. Karanikolos, H. A. Arafat and L. F. Dumee, *J. Environ. Chem. Eng.*, 2023, **11**, 111112.

135 D. Chakraborty, A. Yurdusen, G. Mouchaham, F. Nouar and C. Serre, *Adv. Funct. Mater.*, 2024, **34**, 2309089.

136 L. Zhang, J. Y. Zou and G. X. Peng, *Biol. Chem. Eng.*, 2023, **9**(03), 59–61.

137 M. Taddei, D. A. Steitz, J. A. Bokhoven and M. Ranocchiari, *Chem. - Eur. J.*, 2016, **22**(10), 3245–3249.

138 S. Hübner, S. Kressirer, D. Kralisch, C. Bludszuweit-Philipp, K. Lukow, I. Jänich, A. Schilling, H. Hieronymus, C. Liebner and K. Jähnisch, *ChemSusChem*, 2012, **5**(2), 279–288.

139 M. Shukuya and A. Hammache, 2002: *VTT Technical Research Centre of Finland*.

140 M. Sánchez-Sánchez, N. Getachew, K. Díaz, M. Díaz-García, Y. Chebude and I. Díaz, *Green Chem.*, 2015, **17**(3), 1500–1509.

141 O. Shekhah, H. Wang, D. Zacher, R. A. Fische and C. Wöll, *Angew. Chem., Int. Ed.*, 2009, **48**(27), 5038–5041.

142 J. Huo, M. Brightwell, S. E. Hankari, A. Garai and D. Bradshaw, *J. Mater. Chem. A*, 2013, **1**(48), 15220.

143 W. K. Yu, M. Xu, X. Liang, J. Y. Wang, W. Y. Fang and F. W. Wang, *Sep. Purif. Technol.*, 2022, **303**, 122155.

144 L. Pan, T. Muhammad, L. Ma, Z. F. Huang, S. B. Wang, L. Wang, J. J. Zou and X. W. Zhang, *Appl. Catal. Environ.*, 2016, **189**, 181–191.

145 C. H. Li, C. L. Huang, X. F. Chuah, D. S. Raja, C. T. Hsieh and S. Y. Lu, *Chem. Eng J.*, 2019, **361**, 660–670.

146 A. Pichon, A. Lazuen-Garay and S. L. James, *CrystEng-Comm*, 2006, **8**, 211–214.

147 T. Friscic, D. G. Reid, I. Halasz, R. S. Stein, R. E. Dinnebier and M. J. Duer, *Angew. Chem.*, 2010, **122**, 724–727.

148 G. Lin, B. Zeng, J. Li, Z. Y. Wang, S. X. Wang, T. Hu and L. B. Zhang, *Chem. Eng. J.*, 2023, **460**, 141710.

149 X. Y. Yang, Z. W. Chen, X. Z. Yue, X. Du, X. H. Hou, L. Y. Zhang, D. L. Chen and S. S. Yi, *Small*, 2023, **19**, 2205246.

150 G. A. Tompsett, W. C. Conner and K. S. Yngvesson, *Chem. Phys. Chem.*, 2006, **7**, 296–319.

151 Y. R. Lee, J. Kim and W. S. Ahn, *Korean J. Chem. Eng.*, 2013, **30**, 1667–1680.

152 U. Mueller, M. Schubert, F. Teich, H. Puetter, K. Schierle-Arndt and J. Pastré, *ChemInform*, 2006, **16**, 626–636.

153 U. Müller, M. Schubert, F. Teich, H. Puetter, K. Schierle-Arndt and J. Pastré, *ChemInform*, 2006, **16**, 626–636.

154 Q. Y. Wu, C. X. Zhang, K. Sun and H. L. Jiang, *Acta Chim. Sin.*, 2020, **78**, 688–694.

155 L. Cheng, D. Zhang, Y. Liao, J. Fan and Q. Xiang, *Chin. J. Catal.*, 2021, **42**, 131–140.

156 X. Yue, J. Fan and Q. Xiang, *Adv. Funct. Mater.*, 2022, **32**, 2110258.

157 X. Zhang, D. Xue, S. Jiang, H. Xia, Y. Yang, W. Yan, J. Hu and J. Zhang, *InfoMat*, 2022, **4**, e12257.

158 Y. J. Cheng, J. Q. Zhao, X. F. Ma, H. L. Zheng, L. He, J. Zhang and Q. P. Lin, *Adv. Mater.*, 2025, 2503756.

159 Y. W. Dong, H. J. Liu, X. Wang, F. L. Wang, X. Y. Zhang, Q. X. Lv, C. Y. Liu, Y. M. Chai and B. Dong, *Appl. Catal., B*, 2023, **328**, 122464.

160 Y. Lu, H. X. Zhong, J. Li, A. M. Dominic, Y. M. Hu, Z. Gao, Y. L. Jiao, M. J. Wu, H. Y. Qi, C. H. Huang, L. J. Wayment, U. Kaiser, E. Spiecker, I. M. Weidinger, W. Zhang, X. L. Feng and R. H. Dong, *Angew. Chem., Int. Ed.*, 2022, **61**, e202208163.

161 C. P. Li, S. R. Li, T. X. Hang, F. F. Guo, X. D. Zhu and T. F. Liu, *Small Struct.*, 2022, **3**, 2100071.

162 Y. Q. Liu, X. Xin, Y. H. Shi, Z. F. Zhao, J. D. Tan, D. Yang and Z. Y. Jiang, *Chem. Eng. J.*, 2024, **482**, 149193.

163 R. Tang, S. J. Zhou, L. Y. Zhang and L. W. Yin, *Adv. Funct. Mater.*, 2018, **28**, 1706154.

164 H. J. Hu, X. N. Li, K. L. Zhang, G. Yan, W. X. Kong, A. Q. Qin, Y. L. Ma, A. S. Li, K. Wang, H. W. Huang, X. D. Sun and T. Y. Ma, *Adv. Mater.*, 2025, 2419023.

165 Y. Yang, Q. X. Zhao, Q. Zheng and W. M. Xuan, *J. Donghua Univ.*, 2023, **40**, 590–599.

166 R. H. Li, T. Takata, B. B. Zhang, C. Feng, Q. B. Wu, C. H. Cui, Z. M. Zhang, K. Domen and Y. B. Li, *Angew. Chem., Int. Ed.*, 2023, **62**, e202313537.

167 J. G. Hou, S. Y. Cao, Y. Q. Sun, Y. Z. Wu, F. Liang, Z. H. Lin and L. C. Sun, *Adv. Energy Mater.*, 2018, **8**, 1701114.

168 Y. S. Chen, M. D. Cai, Y. M. Cao, S. S. A. Shuaib, J. Q. Bai, F. Chen, J. W. Xue, Y. X. Wei and S. Sun, *Catal. Sci. Technol.*, 2025, **15**, 3316–3324.

169 Y. R. Song, Y. H. Ren, H. J. Cheng, Y. Y. Jiao, S. B. Shi, L. H. Gao, H. M. Xie, J. F. Gao, L. C. Sun and J. G. Hou, *Angew. Chem., Int. Ed.*, 2023, **62**, e202306420.

170 B. Y. Liu, X. Wang, Y. J. Zhang, L. C. Xu, T. S. Wang, X. Xiao, S. C. Wang, L. Z. Wang and W. Huang, *Angew. Chem., Int. Ed.*, 2023, **62**, e202217346.

171 Y. L. Xin, J. Tian, X. Q. Xiong, C. L. Wu, S. A. C. Carabineiro, X. G. Yang, Z. X. Chen, Y. Xia and Y. X. Jin, *Adv. Mater.*, 2025, **37**, 2417589.

172 J. Wang, K. Liu, W. R. Liao, Y. C. Kang, H. R. Xiao, Y. K. Chen, Q. Y. Wang, T. Luo, J. W. Chen, H. M. Li, T. S. Chan, S. Y. Chen, E. Pensa, L. Y. Chai, F. Y. Liu, L. X. Jiang, C. X. Liu, J. W. Fu, E. Cortés and M. Liu, *Nat. Catal.*, 2025, **8**, 229–238.

173 L. C. Xu, Y. J. Zhang, B. Y. Liu, K. Wan, X. Wang, T. S. Wang, L. Z. Wang, S. C. Wang and W. Huang, *ACS Nano*, 2025, **19**, 15863–15875.

174 P. Y. Dong, J. K. Pan, L. H. Zhang, X. L. Yang, M. H. Xie and J. L. Zhang, *Appl. Catal., B*, 2024, **350**, 123925.

175 S. M. Li, F. Wu, R. B. Lin, J. Wang, C. X. Li, Z. Q. Li, J. Jiang and Y. J. Xiong, *Chem. Eng. J.*, 2022, **429**, 132217.

176 M. Ali, E. Pervaiz, U. Sikandar and Y. Khan, *Int. J. Hydrogen Energy*, 2021, **46**, 18257–18283.

177 D. Kumar, J. E. Abraham, M. Varghese, J. George, M. Balachandran and J. Cherusseri, *Int. J. Hydrogen Energy*, 2024, **50**, 118–141.

178 M. Khosravi and M. R. Mohammadi, *Photosynth. Res.*, 2022, **154**, 329–352.

179 N. Joseph, P. M. Shafi and A. C. Bose, *Energy Fuels*, 2020, **34**, 6558–6597.

180 B. Fabre, C. Falaise and E. Cadot, *ACS Catal.*, 2022, **12**, 12055–12091.

181 M. Fawaz, R. Bahadur, N. P. Dharmarajan, J. H. Yang, C. I. Sathish, A. M. Sadanandan, V. Perumalsamy, G. Singh, X. W. Guan, P. Kumar and A. Vinu, *Carbon*, 2023, **214**, 118345.

182 S. J. Li, L. M. Zhang, W. Q. Zhao, S. H. Yuan, L. Yang, X. Q. Chen, P. Ge, W. Sun and X. B. Ji, *Energy Storage Mater.*, 2020, **32**, 477–496.

183 E. Pervaiz, M. Ali, M. A. Abbasi, T. Noor, Z. Said and H. Alawadhi, *Int. J. Hydrogen Energy*, 2022, **47**, 26915–26955.

184 N. Li, J. Liu, B. X. Dong and Y. Q. Lan, *Angew. Chem., Int. Ed.*, 2020, **59**, 20779–20793.

185 R. Kulkarni, L. P. Lingamdinne, R. R. Karri, Z. H. Momin, J. R. Koduru and Y. Y. Chang, *Coordin. Chem. Rev.*, 2023, **497**, 215460.

186 W. J. Liu, F. Qiao, J. Yang, J. R. Yuan, Y. Xie, T. Wang, J. Z. Hu, J. H. Zheng, R. Ren, X. M. Kang, Y. Zhao and J. W. Zhang, *Nano Res.*, 2023, **16**, 10401–10411.

187 H. H. Hu, Z. Y. Wang, L. Y. Cao, L. Z. Zeng, C. K. Zhang, W. B. Lin and C. Wang, *Nat. Chem.*, 2021, **13**, 358–366.

188 D. Wang, J. L. Gu, H. L. Wang, M. Z. Liu, Y. H. Liu and X. T. Zhang, *Appl. Surf. Sci.*, 2023, **619**, 156710.

189 Q. C. Lin, W. M. Liao, J. Y. Li, B. W. Ye, D. T. Chen, X. X. Zhou, P. H. Li, M. Li, M. D. Li and J. He, *Angew. Chem., Int. Ed.*, 2025, **64**, e202423070.

190 Z. Y. Zhou, Y. N. Xie, W. Z. Zhu, H. Y. Zhao, N. J. Yang and G. H. Zhao, *Appl. Catal., B*, 2021, **286**, 119868.

191 S. Kim, D. S. Han and H. Park, *Appl. Catal., B*, 2021, **284**, 119745.

192 C. Liu, D. Fu and H. Li, *Environ. Technol.*, 2012, **33**(7), 791–799.

193 J. Y. Sun, H. Maimaiti, B. Xu, L. R. Feng, J. Z. Bao and X. W. Zhao, *Appl. Surf. Sci.*, 2022, **585**, 152701.

194 Y. C. Miao and M. F. Shao, *Chin. J. Catal.*, 2022, **43**, 595–610.

195 Y. Z. Zhang, Y. R. Dai, H. H. Li, L. F. Yin and M. R. Hoffmann, *Commun. Mater.*, 2020, **1**, 66.

196 S. Ye, W. H. Feng, J. J. Li, H. Y. Zhong, J. Y. Weng and H. Li, *J. Electroanal. Chem.*, 2022, **927**, 116975.

197 C. H. Zhou, J. H. Li, J. C. Wang, C. Y. Xie, Y. Zhang, L. Li, T. S. Zhou, J. Bai, H. Zhu and B. X. Zhou, *Appl. Catal., B*, 2023, **324**, 122229.

198 K. Iwashina, A. Iwase, Y. H. Ng, R. Amal and A. Kudo, *J. Am. Chem. Soc.*, 2015, **137**, 604–607.

199 M. Fekete, W. Riedel, A. F. Patti and L. Spiccia, *Nanoscale*, 2014, **6**, 7585–7593.

200 Z. Y. Zhou, Y. N. Xie, W. Z. Zhu, H. Y. Zhao, N. J. Yang and G. H. Zhao, *Appl. Catal., B*, 2021, **286**, 119868.

201 Z. A. Huang, Z. Z. Wang, H. Rabl, S. Naghdi, Q. C. Zhou, S. Schwarz, D. H. Apaydin, Y. Yu and D. Eder, *Nat. Commun.*, 2024, **15**, 9393.

202 J. J. Zhang, T. Y. Bai, H. Huang, M. H. Yu, X. B. Fan, Z. Chang and X. H. Bu, *Adv. Mater.*, 2020, **32**, 2004747.

203 H. Wang, X. K. Liu, Y. L. Zhao, Z. H. Sun, Y. Lin, T. Yao and H. L. Jiang, *Nat. Sci. Rev.*, 2024, **11**, 252.

204 S. Naghdi, A. Cherevan, A. Giesriegl, R. Guillet-Nicolas, S. Biswas, T. Gupta, J. Wang, T. Haunold, B. C. Bayer, G. Rupprechter, M. C. Toroker, F. Kleitz and D. Eder, *Nat. Commun.*, 2022, **13**, 282.

205 K. Li, J. Yang and J. L. Gu, *Acc. Chem. Res.*, 2022, **55**(16), 2235–2247.

206 D. X. Yang, Q. Z. Xiong, Y. Wang, Y. Chen, L. B. Li and J. P. Li, *Chem. Ind. Eng. Prog.*, 2024, **43**(04), 1882–1896.

207 Y. Yao, X. Y. Zhao, G. G. Chang, X. Y. Yang and B. L. Chen, *Small*, 2023, **4**, 2200187.

208 W. G. Huang, B. Chan, Y. W. Yang, P. Chen, J. J. Wang, L. Casey, C. Atzori, T. Schulli, O. Mathon, H. G. Hackbarth, N. M. Bedford, D. Appadoo, X. M. Li, T. G. Lin, R. J. Lin, J. Lee, Z. L. Wang, V. Chen, A. K. Cheetham, L. Z. Wang and J. W. Hou, *J. Am. Chem. Soc.*, 2025, **147**, 3195–3205.

209 H. H. Hu, Z. Y. Wang, L. Y. Cao, L. Z. Zeng, C. K. Zhang, W. B. Lin and C. Wang, *Nat. Chem.*, 2021, **13**, 358–366.

210 B. B. Chen, D. Fan, R. V. Pinto, I. Dovgaliuk, S. Nandi, D. Chakraborty, N. G. Moncada, A. Vimont, C. J. McMonagle, M. Bordonhos, A. A. Mohtar, I. Cornu, P. Florian, N. Heymans, M. Daturi, G. D. Weireld, M. Pinto, F. Nouar, G. Maurin, G. Mouchaham and C. Serre, *Adv. Sci.*, 2024, **11**, 2401070.

211 D. Senthil Raja and D. H. Tsai, *Chem. Commun.*, 2024, **60**, 8497–8515.

212 H. Y. Chu, Z. X. Liu, C. C. Wan and P. Wang, *Chem. Commun.*, 2024, **60**, 8350–8359.